Amplitude and phase modes in *trans*-polyacetylene:
Resonant Raman scattering and induced infrared activity

E. Ehrenfreund, Z. Vardeny, and O. Brafman

Department of Physics and Solid State Institute, Technion–Israel Institute of Technology, Technion City, 32 000 Haifa, Israel

B. Horovitz

Department of Physics, Ben Gurion University of the Negev, 84 105 Beer-Sheva, Israel

The resonant Raman scattering (RRS) from the three A_g modes of *trans*-polyacetylene and the charged-induced ir modes are analyzed with use of the amplitude- and phase-mode theories. It is shown that the observed phonon frequencies and the relative intensities of all modes obtained at various laser excitation energies $\hbar\omega_L$ is accounted for by a single phonon propagator which also describes the charge-induced infrared-active modes. The dispersion of the RRS frequencies with $\hbar\omega_L$ exhibits inhomogeneity of the sample which in turn provides the functional dependence of the π-electron gap E_g on an effective coupling parameter $\tilde{\lambda}$. We show that inhomogeneity in both the electron-phonon and the electron-electron interaction parameters yields inhomogeneity in $\tilde{\lambda}$. The experimental gap-versus-$\tilde{\lambda}$ relation is consistent with the Peierls model but allows for weak electron-electron interactions which enhance the gap. We propose a method by which the distribution in $\tilde{\lambda}$, $P(\tilde{\lambda})$, is directly *derived* from the experimental spectra. It appears that different samples show different breadth for the distribution function; samples with sharper RRS features have narrower $P(\tilde{\lambda})$. We give an experimental estimate of the σ-bond contribution to the force constant of the carbon-carbon stretching mode and the electron-phonon interaction parameter. The pinning parameter of the charged carriers and its distribution are *derived* directly from the infrared absorption spectra induced either by doping or by photogeneration. The pinning of the doping-induced carriers is stronger and its distribution is wider; giving thus rise to the broader lines in the doping-induced infrared spectra. The mass of the photogenerated solitons is estimated from the relative strength of the infrared spectra and is approximately equal to the band effective mass of the electrons.

I. INTRODUCTION

Resonant Raman scattering (RRS) has been extensively used in recent years to study the inhomogeneity and disorder of *trans*-polyacetylene. The Raman spectrum of *trans*-polyacetylene has by now been measured on many different samples by various groups,[1–4] and it has several unique features. As the incident laser photon energy ($\hbar\omega_L$) is increased from deep-red, the RRS bands change gradually from a narrow, slightly asymmetric line into a more-complicated two-peak band consisting of an unshifted primary peak and an upward shifted satellite portion which becomes the prominent feature of the band at deep-blue and uv excitations (see Fig. 1). The exact shape of the RRS bands depends strongly on sample quality: "better" samples show sharper double-peak features. However, the position of the primary and the satellite peaks are sample independent. These distinctive features have been regarded as evidence for the presence of inhomogeneity (or disorder) in *trans*-polyacetylene. The disorder results in a distribution of the electronic energy gaps and the respective frequencies, which are selectively probed by the RRS process, leading to the shift and broadening of the phonon bands.

In early attempts to account for the RRS features, the inhomogeneity was attributed to a distribution of chains

with varying length of π-electron conjugation.[2,3] In this approach (using either the particle-in-the-box model[3,5] or Hückel-type calculations[6,7]) chains with shorter conjugation length have larger electronic gap, thereby becoming selectively probed at higher laser excitation energies. In addition, based on the observation in finite polyene chains,[8] the phonon frequencies are assumed to increase with decreasing conjugation length. The satellite peak in that model is then assumed to result from a considerable amount of chains with short conjugation length. Using this model to fit the RRS spectra in detail, several authors[6,9,10] have inferred that the disorder in *trans*-polyacetylene is caused by a double-peak distribution of conjugation lengths: one peak corresponds to relatively long (>200 carbon atoms) chains, while the other is due to a substantial amount of chains with short (10–20 C atoms) conjugation length.

In a more general point of view the skeleton chain (i.e., without π electrons) has a few "bare" normal modes which have the right symmetry to induce dimerization (there are three such modes in *trans*-polyacetylene). The coupling of the π electrons to these normal modes drives the dimerization, and each normal mode becomes a symmetric vibration of the dimerization amplitude—a Raman-active "amplitude mode."[11–13] The restoring force of these vibrations is associated with the dimeriza-

tion mechanism itself, i.e., the coupled electron-phonon system resists changes in the dimerization amplitude.

When charge carriers are added to the chain the translational symmetry of the system is broken. New normal modes ("phase modes") which are related to the translational degree of freedom of the charge, become infrared (ir) active and they describe charge oscillations.[14] The limit of many excess charges is the incommensurate case with similar ir activity.[15] Each bare mode results in an infrared-active vibration with restoring force given by the "pinning" potential which resists the charge translation. In particular, in a perfectly translationally invariant system (i.e., no pinning potential) the lowest-frequency mode, commonly called the "pinned mode," shifts down to zero frequency.

Experimentally, by adding a charge onto the chain, either by doping or by photogeneration, several ir-active vibrations (IRAV) were observed[1,16−21] (Fig. 2). The observed IRAV lines induced by photogeneration are correspondingly lower in frequency than those induced by doping. The IRAV spectra were originally attributed[16] to molecular vibrations made ir active by the added charge and subsequently were considered[18,22] as an evidence for the soliton defect.[23−26] However, as was shown by one of us,[14] these IRAV modes are a universal result of the translation degree of freedom for the added charge, independent of its configuration. It was also shown that the doping-induced ~ 900-cm^{-1} mode in trans-$(CH)_x$ [or the ~ 750-cm^{-1} mode in trans-$(CD)_x$ (see Fig. 2)] is the "pinned" mode which indeed shifts down[21] to ~ 500 cm^{-1} for the more weakly pinned photogenerated charges.
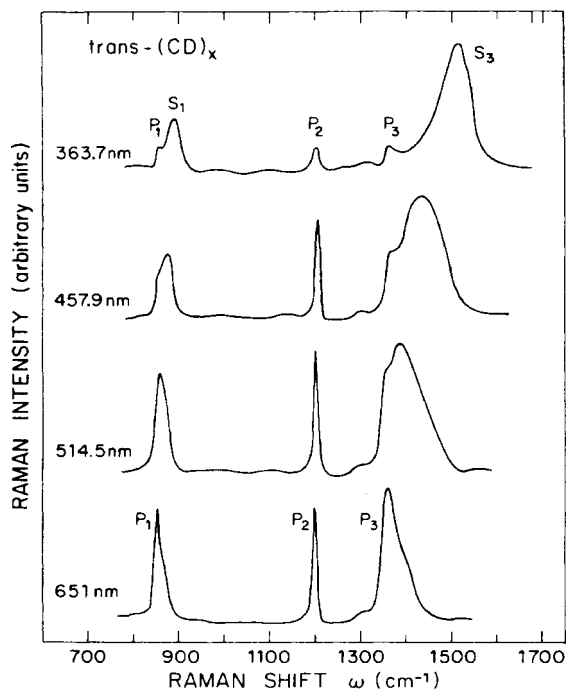
In previous reports[28,29] we have applied the amplitude-mode (AM) approach to trans-polyacetylene and have shown that the behavior of the RRS as well as the IRAV spectra can indeed be accounted for in detail. We have found also that the disorder in trans-polyacetylene can be described as a distribution $P(\tilde{\lambda})$ of a dimensionless effective coupling parameter $\tilde{\lambda}$. Furthermore, unlike the conjugation length models, our derived $P(\tilde{\lambda})$ is a single-peak distribution, and the existence of chains with very short conjugation lengths in the material is not a necessary condition to account for the dispersion of the RRS lines. In addition, we have concluded that the measured gap E_g in the range of 1.8–3.5 eV is consistent with a Peierls-type relation in $\tilde{\lambda}$, i.e., $E_g \sim \exp(-1/2\tilde{\lambda})$.

The purpose of this paper is to elaborate on the RRS and the IRAV analysis in terms of the amplitude- and phase-mode theories, and to extend our earlier conclusions by including electron correlation effects. The paper is organized as follows. In Sec. II we describe the relevant part of the amplitude-mode theory for the interpretation of the Raman and charge-induced infrared data of trans-polyacetylene, including the treatment of finite chains in the Hückel approximation and the effect of electron-electron interaction. In Sec. III we analyze in detail the Raman data using the amplitude-mode theory and show that the observed spectra are Raman scattering from amplitude modes. Using the experimental RRS spectrum we show how to derive the distribution function $P(\tilde{\lambda})$ for inhomogeneous samples. The amplitude-mode theory, together with the distribution of the effective coupling parameter $\tilde{\lambda}$, can account for the frequencies, relative intensities, shape, width, excitation profile of the Raman lines, and the dispersion with the incoming laser photon energy. In Sec. IV we analyze the IRAV data and show that the phase-mode theory reproduces all the details of the IRAV spectrum with one additional pinning parameter. In Sec. V we analyze the functional depen-
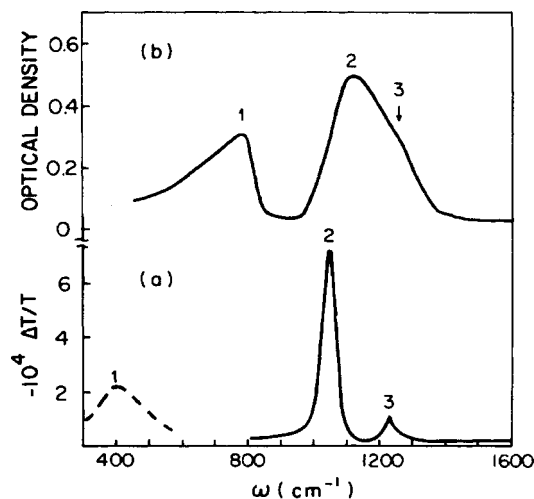

FIG. 1 Resonant Raman spectra of trans-$(CD)_x$ at 300 K. The symbols P and S denote primary and satellite lines, respectively.

FIG. 2. IRAV spectra of trans-$(CD)_x$. (a) Photogenerated ir absorption of an undoped sample (Ref. 20). The arrow at 400 cm^{-1} indicates the position of the pinning mode (Ref. 21). (b) ir absorption of lightly doped AsF_5 sample (Ref. 18).

dence between $\tilde{\lambda}$ and the gap and show that the electron correlations may play an important role in *trans*-$(CH)_x$. We also give estimates for the σ-bond force constant and the electron-phonon interaction.

II. THEORETICAL CONCEPTS

A. A single-phonon case

The dimerization of long conjugated molecules such as polyacetylene has long been known to be the result of a delicate balance between the decrease in the energy E_π of the π electrons and the increase of the σ-electron elastic energy E_σ upon dimerization.[30] Defining the dimerization amplitude u as half the difference between the lengths of the single and double bonds projected in the chain direction, we schematically plot (for weak e-ph coupling) in Fig. 3 the energies E_σ (curve a) and E_π (curve b) and the total energy $E_T = E_\sigma + E_\pi$ (curve c) as a function of u for *trans*-$(CH)_x$. Positive and negative values of u refer to "right" and "left" dimerization patterns, as shown in the insets of Fig. 3. It is seen that equilibrium occurs for $u \neq 0$ and that the curvature $\partial^2 E_T / \partial u^2$ at the energy minimum of the total energy is smaller than that of the elastic energy. Furthermore, since $E''_\pi < 0$ (at least near the maximum, i.e., in weak coupling), it is readily seen that $\partial^2 E_T / \partial u^2 < \partial^2 E_\sigma / \partial u^2$ even for cases where equilibrium occurs for $u = 0$, i.e., even when the system is undimerized. In other words, the force constants (and consequently the vibrational frequencies) are reduced due to the
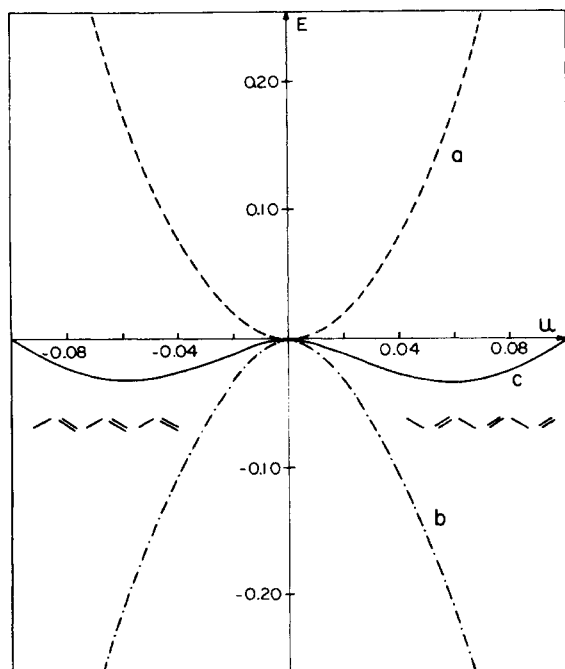

FIG. 3. Schematic energy-dimerization diagram for *trans*-$(CH)_x$. a, σ-electron elastic energy; b, π-electron energy; and c, total energy. The inset shows the two degenerate ground-state dimerization patterns.

π electrons by an amount proportional to $|E''_\pi|$. Thus in the case of a single-vibrational-mode system the vibration frequency ω is lower than the elastic (or "bare") vibration frequency ω_0:

$$\omega^2 = \omega_0^2 - (\omega_0^2 / K) |E''_\pi| , \tag{1}$$

where $K = d^2 E_\sigma / du^2$ is the elastic force constant (due to the potential of the σ electrons). The vibrational force constant is thus reduced, with respect to the elastic force constant K, by a factor $2\tilde{\lambda}$ given by

$$2\tilde{\lambda} = \omega^2 / \omega_0^2 = 1 - |E''_\pi| / K . \tag{2}$$

When the system is dimerized (i.e., $u \neq 0$ in equilibrium), a dimerization gap $2\Delta_d$ is opened in the π-electron system. If e-e interactions are not included (however, see Sec. II F), this gap is given by $2\Delta_d = 8\beta u$ where β is the linear electron-phonon (e-ph) interaction. Thus, the vibrational mode of the dimerized chain reflects oscillations of the π-electron dimerization gap and is then an amplitude mode around the static configuration of the dimerized lattice. In weak coupling we expect $2\tilde{\lambda} < 1$ and an amplitude-mode frequency less than ω_0. Note that E_π may depend on e-e interaction and disorder, so that Eq. (2) is a general result for an adiabatic single-phonon case.

B. The multiphonon case

In this section we review the amplitude-mode formalism developed earlier by one of us.[14] Consider N_m phonon normal modes in a uniformly dimerized infinite chain. These $q = 0$ phonons correspond to time-dependent fields $\Delta_n(t)$, $n = 1, 2, \ldots, N_m$. They couple to the electrons by the interaction Hamiltonian

$$H_{e\text{-ph}} = \sum_{n=1}^{N_m} \Delta_n(t)(C + C^\dagger) , \tag{3}$$

where C involves π-electron operators describing scattering between opposite sides of the Fermi surface. For bond dimerization, as in *trans*-$(CH)_x$, $C = \sum_m (-1)^m C_m^\dagger C_{m+1}$ where $C_m^\dagger$ creates an electron at site m. Modes which couple to site dimerization, i.e., $C = \sum (-1)^m C_m^\dagger C_m$ are ignored in this scheme. The presence of such modes does not affect the following Raman analysis,[31] but may affect the analysis of the induced ir spectra.

To identify the various modes in *trans*-$(CH)_x$, note first that modes which lead to either bond or site dimerization break the glide line symmetry of the chain (if the chain was straight rather then zigzag, then these modes would be at the Brillouin zone boundary). There are four such modes corresponding to the in-plane oscillations of the C and H atoms. The inversion center at a bond center determines three of these modes to be symmetric;[32] i.e., having the symmetry of bond dimerization, while one mode is antisymmetric,[32] having the symmetry of site dimerization. The latter mode is a C–H–type vibration at ~ 3000 cm^{-1} and is very weakly coupled to the π electrons. The fields Δ_n and the normal mode displacement u_n are proportional through the dimensionless electron-phonon coupling constant for each mode (λ_n)

$$\Delta_n = \left[\frac{\mu_n (\omega_n^0)^2 \lambda_n}{2N(0)} \right]^{1/2} u_n \ , \tag{4}$$

where ω_n^0 are the bare frequencies, i.e., the normal-mode frequencies in the absence of the π electrons. μ_n are the mode reduced mass and $N(0)$ is the electron density of states at the Fermi energy. The electrons then respond by Eq. (3) to the combination field $\Delta(t) = \sum_n \Delta_n(t)$.

Define now the expectation value of the total π-electron energy E_π as the sum of the electron kinetic energy (el), electron-electron (e-e), electron-phonon (e-ph) interactions, and disorder term (dis) by

$$E_\pi = \langle H_{el} + H_{e\text{-}e} + H_{e\text{-}ph} + H_{dis} \rangle \equiv -N(0)E_i(\Delta) \ . \tag{5}$$

In the adiabatic limit, i.e., all phonon frequencies ω_n are much lower than the electronic energy gap E_g, E_i does not depend on time derivative $\dot{\Delta}$ but on $\Delta(t)$ only. This is the single assumption in the theory, and is valid for polyacetylene since $\omega_n / E_g < 0.1$ (Ref. 14).

The total-energy density for the combined electron-phonon system is now

$$E_T = N(0) \left[\sum (4\lambda_n)^{-1} \left| \frac{\dot{\Delta}_n^2}{(\omega_n^0)^2} + \Delta_n^2 \right| - E_i(\Delta) \right] \ , \tag{6}$$

where we have used Eq. (4) to write the kinetic and potential energies of the bare phonons in terms of Δ_n. Minimizing Eq. (6) with respect to Δ_n, we obtain $\Delta_n^0 = 2\lambda_n E_i'(\Delta_0)$ with $\Delta_0 = \sum_n \Delta_n^0$. Therefore, the ground-state gap parameter Δ_0 is given by

$$\Delta_0 = 2\lambda E_i'(\Delta_0) \ , \tag{7}$$

where $\lambda = \sum_n \lambda_n$ and $\Delta_n^0 = \Delta_0 \lambda_n / \lambda$. To obtain the phonon modes we assume small oscillations around the ground state: $\Delta_n(t) = \Delta_n^0 + \gamma_n(t)$ and expand the total-energy density Eq. (6) keeping terms to second-order only. These terms yield the effective classical Hamiltonian for the phonon modes

$$H\{\gamma_n\} = N(0) \left[\sum (4\lambda_n)^{-1} \left| \frac{\dot{\gamma}_n^2}{(\omega_n^0)^2} + \gamma_n^2 \right| \right.$$
$$\left. - \tfrac{1}{2} E_i''(\Delta_0)\gamma^2 \right] \ , \tag{8}$$

where $\gamma(t) = \sum_n \gamma_n(t)$. Note that the second derivative E_i'' acts as an extra potential-energy term, thereby renormalizing the bare phonon modes of the system. Equation (8) yields N_m coupled equations of motion with eigenfrequencies given by the solution of the following equation:[29]

$$D_0(\omega) = -(1 - 2\tilde{\lambda})^{-1} \ , \tag{9}$$

where the phonon propagator $D_0(\omega)$ is given by

$$D_0(\omega) = \sum \frac{\lambda_n}{\lambda} \frac{(\omega_n^0)^2}{\omega^2 - (\omega_n^0)^2 - i\omega\delta_n} \tag{10}$$

and the renormalization coupling parameter $\tilde{\lambda}$ is defined by

$$2\tilde{\lambda} = 1 - 2\lambda E_i''(\Delta_0) \ . \tag{11}$$

Note that Eq. (11) is the same as Eq. (2) of the single-mode theory. Figure 4(a) shows the form of $D_0(\omega)$ for three coupled modes; a given coupling parameter $\tilde{\lambda}$ defines a horizontal line at $-(1 - 2\tilde{\lambda})^{-1}$ and its intersection with $D_0(\omega)$ [Eq. (9)] yields the renormalized frequencies. These frequencies correspond to spatially uniform oscillations in the amplitude of the dimerization; being symmetrical modes, they are Raman active.

Equation (9) is an N_mth-order polynomial equation in ω^2 which thus can be written in the form $\pi(\omega^2 - \omega_n^2) = 0$ where ω_n are the roots of the equation. Comparing these two forms of Eq. (9), we obtain a useful "product rule,"[14]

$$\prod_{n=1}^{N_m} (\omega_n / \omega_n^0)^2 = 2\tilde{\lambda} \ . \tag{12}$$

Note that the amplitude-mode formalism described in this section includes electron-electron interaction and effects of disorder in an implicitly way via $E_i(\Delta)$. In the following sections we treat specific examples of chains with various types of interactions.

C. Peierls chains

When the electron-electron interaction is neglected, the total π-electron energy, and hence $E_i(\Delta)$, can be calculated and expressed in a closed form. For an infinitely long uniform chain the energy levels in the tight-binding or
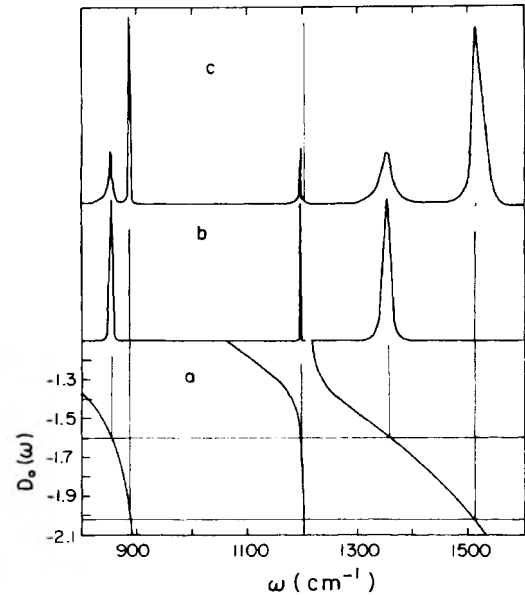

FIG. 4. a, The function $D_0(\omega)$ [Eq. (10)]. The horizontal line represents $-(1 - 2\tilde{\lambda})^{-1}$ or $-(1 - \alpha)^{-1}$ for determining the Raman or ir modes, respectively. b, Calculated RRS spectrum of a three-oscillator inhomogeneous system with a single-peak distribution function $P(\tilde{\lambda})$, and negligible natural phonon width. The resonance condition corresponds to the peak of $P(\tilde{\lambda})$. c, Same as b, but for resonance away from the peak of $P(\tilde{\lambda})$ (see text).

Hückel approximation are given by

$$\varepsilon_k^0 = -2t\cos(ka) \ ,\tag{13}$$

where t is the nearest-neighbor transfer integral, a is the lattice constant, and k is the one-dimensional wave vector. In the commensurate case with one electron per atom the Fermi energy is at $\varepsilon = 0$ and the dimerized state is characterized by two different nearest-neighbor transfer integrals t_1 and t_2. In the weak-coupling limit $|t_1 - t_2| = 4\sum_n \beta_n u_n$, where β_n is the change in the transfer integral due to a unit displacement of the mode n. Identifying Δ_n of Eq. (3) with $4\beta_n u_n$, we see that the electrons are coupled to the phonons via the field

$$\Delta = 4\sum_n \beta_n u_n \ .\tag{14}$$

With the dimerization Δ taking place, the electron energy levels become[30]

$$\varepsilon_k = \pm 2t[\cos^2(ka/2) + (\Delta/2t)^2]^{1/2} \ ,\tag{15}$$

where in Eq. (15) $t = (t_1 t_2)^{1/2}$, and E_i is now given by

$$E_i(\Delta) = \sum_k (\,|\varepsilon_k| - |\varepsilon_k^0|\,)/N(0) \ .\tag{16}$$

With $N(0) = (\pi t a)^{-1}$ for the tight-binding approximation, we find

$$E_i(\Delta) = 4t^2[1 + (\Delta/2t)^2]^{1/2}E \ ,\tag{17}$$

where E is the complete elliptic integral of the second kind with an argument $\kappa = [1 + (\Delta/2t)^2]^{-1/2}$. The value of the π-electron binding energy $E_\pi = -\pi t E_i$ is in agreement with that of Ref. 30. For $\Delta \ll 2t$ we obtain, by neglecting terms of order higher than $(\Delta/2t)^2$, the familiar form[14,33]

$$E_i(\Delta) = \Delta^2/4 + (\Delta^2/2)\ln(2E_c/\Delta) \ ,\tag{18}$$

where $E_c = 4t$ is an "electron cutoff energy." The form (18) for the dependence of E_i on Δ (for $\Delta \ll E_c$) is independent of the dispersion relation ε_k^0 for the uniform chain; however, the actual value of E_c does depend on ε_k^0. For a linear dispersion $\varepsilon_k^0 = \hbar v_F k$, $E_c = \hbar v_F k_F$ (Refs. 25 and 33), whereas for the free-electron chain with $\varepsilon_k^0 = \hbar^2 k^2/2m$, $E_c = 2\varepsilon_F$ (Ref. 34), where v_F and ε_F are the Fermi velocity and energy, respectively.

Equation (17) then yields for the gap equation of the infinite chain

$$(2\lambda)^{-1} = K(\kappa) \ ,\tag{19}$$

where K is the complete elliptic integral of the first kind with an argument $\kappa = [1 + (\Delta/2t)^2]^{1/2}$. For $\Delta_0 \ll 2t$ we obtain the Peierls relation for the gap

$$\Delta_0 = 2E_c\exp(-1/2\lambda) \ .\tag{20}$$

For a finite polyene chain with N carbon atoms, the bonding and antibonding orbital energies are also given by Eq. (15) with N discrete values of k. For an odd chain there is an additional nonbonding orbital at $\varepsilon = 0$. $E_i(\Delta)$ is given by Eq. (16) with $N(0) = (\pi t a)^{-1}$. In general, closed-form formulas for $E_i(\Delta)$ and its derivatives cannot be given and they should be computed numerically. It

should be emphasized, however, that whereas for the infinite chain case the electronic gap in the dimerized state was given by $2\Delta_0$, here the discreteness of the levels leads to a minimum separation E_g between bonding and antibonding orbitals given by

$$E_g = 4t[\cos^2\phi_N + (\Delta/2t)^2]^{1/2} \ ,\tag{21}$$

where ϕ_N is determined by the chain length; for even cyclic chains $\phi_N = (1 - 2/N)\pi/2$. The gap parameter Δ is, in general, a function of N and its equilibrium value Δ_0 is determined by Eq. (7).

An important experimental parameter is $\bar{\lambda}$ [Eq. (11)], which can be determined from the observed Raman frequencies using the product-rule relation, Eq. (12). For the infinite chain we find $\bar{\lambda} = \lambda$; thus the RRS frequencies yield the *e*-ph coupling parameter λ. Numerical calculations for finite chains show that $\bar{\lambda}(N) < \lambda$ and increases as N increases. Recalling that in finite chains the RRS frequencies (and hence $\bar{\lambda}$) decrease with chain length, we must conclude that either Coulomb interactions are significant or the parameters λ and t are N dependent; e.g., a decreasing $\bar{\lambda}(N)$ could overcome the "bare" (i.e., with λ and t fixed) N dependence.

D. Cross section for Raman scattering from amplitude modes

Conventionally, the Raman cross section for molecules or polymers is expressed in terms of the electronic excited-state parameters.[2–7,9,10] In another approach, used primarily in semiconductors, one uses ground-state wave functions and the *e*-ph coupling constant λ to express the Raman cross section. While the two methods are equivalent, the latter is preferred in our quasi-one-dimensional case since it explicitly shows the divergence of the Raman cross section near the band edge and the coupling between the various vibrational modes inherent to the AM analysis. The form of the cross section for the Peierls model is calculated in Appendix A utilizing the frequency-dependent electronic conductivity of the Peierls semiconductor. The result is[29a]

$$\frac{d^2\sigma}{d\Omega\,d\omega} \propto \frac{\lambda}{E_g^2}\left|f\left|\frac{\hbar\omega_L}{E_g}\right|\right|^2 \mathrm{Im}\left|\frac{-D_0(\omega)}{1 + (1 - 2\bar{\lambda})D_0(\omega)}\right| ,\tag{22}$$

where the ω dependence is contained only in the second factor, which is the propagator for the amplitude modes. The matrix-element function $f(\hbar\omega_L/E_g)$ contains the resonance effect, i.e., it reaches its maximum at $\hbar\omega_L = E_g$ and it is independent of the Raman frequency shift ω if $\hbar\omega \ll \hbar\omega_L$, $|\hbar\omega_L - E_g|$. A detailed derivation is given in Appendix A where it is shown that for a one-dimensional (1D) Peierls chain f is given by[29(b)]

$$f(x) = -\frac{1}{1-x^2} + \frac{1-2x^2}{x(1-x^2)^{3/2}}$$

$$\times\tan^{-1}\left|\frac{x}{(1-x^2)^{1/2}}\right| , \quad x < 1\tag{23}$$

and

$$f(x) = \frac{1}{x^2 - 1} + \frac{2x^2 - 1}{2x(x^2 - 1)^{3/2}}$$

$$\times \left| \ln \left| \frac{x - (x^2 - 1)^{1/2}}{x + (x^2 - 1)^{1/2}} \right| + \pi i \right|, \quad x > 1 \quad (24)$$

where $x = \hbar\omega_L / E_g$. The function $f(x)$ given in Eqs. (23) and (24) strongly diverges at resonance $(x = 1)$ due to the singularity of the 1D density of states at the band edge. In a real system, like polyacetylene, finite interchain coupling leads to a modified density of states in the vicinity of the band edge;[35–37] the divergence is smeared to a finite peak with width $\sim W_\perp$, the transverse bandwidth. The function $f(x)$ and the Raman scattering cross section become finite. Although the detailed shape of $f(x)$ near resonance depends on the detailed three-dimensional band structure, it should be smooth function peaked at $x = 1$. We have therefore approximated $f(x)$ near resonance by a function with a finite peak at $x = 1$ (e.g., a Gaussian) and connected it smoothly to the one-dimensional $f(x)$ [Eqs. (23) and (24)] at $|\hbar\omega_L - E_g| = W_\perp$. An example of an approximation to $f(x)$ which has been used for fitting the RRS data of trans-polyacetylene is shown in Fig. 5.

The propagator for the amplitude modes in Eq. (19) yields the position, width, and relative intensities of the various Raman lines. When the natural phonon widths are small, the position of each line, ω_n, is given by the poles of Eq. (22), while the intensity I_n is proportional to the residue at the poles, i.e.,

$$I_n \propto \left| \frac{\partial D_0(\omega)}{\partial \omega} \right|_{\omega = \omega_n}^{-1}. \quad (25)$$

E. Inhomogeneous systems

So far we have assumed a homogeneous quasi-one-dimensional system for which the chain parameters (λ, t, $\tilde{\lambda}$, etc.) are spatially uniform. A static inhomogeneity (caused, for instance, by variable chain length, bond length disorder, etc.) can be incorporated into the condensation energy function $E_i(\Delta)$ resulting in a spatial distribution of the internal chain parameters. From RRS experiments one determines two of these parameters: E_g and $\tilde{\lambda}$. E_g is obtained from the resonance effect $\hbar\omega_L = E_g$, and $\tilde{\lambda}$ from the measured RRS frequencies, using either Eq. (9) or the product-rule relation Eq. (12). Thus by selectively probing various regimes in the distribution, an inhomogeneous system can provide directly the relation between $\tilde{\lambda}$ [or $E_i''(\Delta)$, Eq. (11)] and E_g [or $E_i'(\Delta)$, Eqs. (7) and (21)], which can be compared with models for $E_i(\Delta)$ (e.g., Peierls, electron-electron interaction, extrinsic gaps, etc.).

It is convenient to characterize the inhomogeneity of the system by a distribution function $P(\tilde{\lambda})$ in the renormalization coupling constant $\tilde{\lambda}$. The distribution in $\tilde{\lambda}$ translates into a distribution in the gap via Eqs. (7), (11), and (21). The Raman cross section is then obtained by integrating the cross section [Eq. (A4), Appendix A] over $\tilde{\lambda}$:
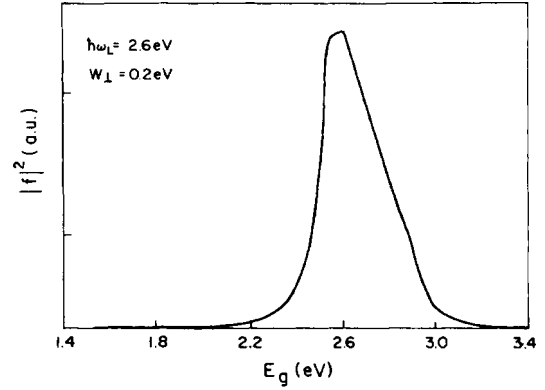

FIG. 5. The function $|f(\hbar\omega_L / E_g)|^2$ as a function of E_g for $\hbar\omega_L = 2.6$ eV and $W_\perp = 0.3$ eV.

$$\frac{d^2\sigma}{d\Omega\, d\omega} \propto \int d\tilde{\lambda}\, P(\tilde{\lambda}) \frac{\lambda}{E_g^2} \left| f\left| \frac{\hbar\omega_L}{E_g} \right| \right|^2$$

$$\times \mathrm{Im} \left| \frac{-D_0(\omega)}{1 + (1 - 2\tilde{\lambda})D_0(\omega)} \right|, \quad (26)$$

where $\int P(\tilde{\lambda})d\tilde{\lambda} = 1$. Equation (26) predicts several important characteristics of the Raman spectrum regardless of the type of the interaction. Defining $\tilde{g}(\omega) = 1 + (1 - 2\tilde{\lambda})D_0(\omega)$, we see that for negligible natural phonon width [$\delta_n \sim 0$ in Eq. (10)] one can approximate the amplitude-mode propagator by a sum of δ functions:

$$\mathrm{Im} \left| \frac{-D_0(\omega)}{1 + (1 - 2\tilde{\lambda})D_0(\omega)} \right| \simeq -D_0(\omega)\delta[\tilde{g}(\omega)]$$

$$= \frac{1}{2} \sum_n \frac{\delta(\omega - \omega_n)}{(1 - 2\tilde{\lambda})^2 D_0'(\omega_n)}. \quad (27)$$

The last equality is obtained using Eq. (9) for the Raman lines: $D_0(\omega) = -(1 - 2\tilde{\lambda})^{-1}$, where ω_n are the observed RRS frequencies. Consequently, the expression for the RRS cross section of an inhomogeneous system [Eq. (26)] can be integrated to yield a very simple form:

$$\frac{d^2\sigma}{d\Omega\, d\omega} \propto \frac{\lambda}{E_g^2(\tilde{\lambda}_\omega)} \left| f\left| \frac{\hbar\omega_L}{E_g(\tilde{\lambda}_\omega)} \right| \right|^2 P(\tilde{\lambda}_\omega), \quad (28)$$

where $2\tilde{\lambda}_\omega = 1 + D_0^{-1}(\omega)$. Equation (8) predicts the following features in the Raman spectrum. (a) In the case of a multiphonon system all the Raman lines are of equal height while their total intensity (and therefore their width) is proportional to $[D_0'(\omega)]^{-1}$, as seen in Fig. 4(b). (b) Each of the Raman lines is double peaked: a primary line which corresponds to the maximum of $P(\tilde{\lambda})$ at $\tilde{\lambda} = \tilde{\lambda}_0$ and a satellite line at a frequency which corresponds to the maximum in $f(x)$, i.e., to the resonance condition $\hbar\omega_L = E_g(\tilde{\lambda}) > E_g(\tilde{\lambda}_0)$. This is shown in Fig. 4(c), where the primary lines do not shift with the laser excitation energy and the satellite lines shift upward with increasing ω_L. Note again the equal heights of all three primary Raman lines and of all three satellite

lines. The equal heights are the result of the negligible natural width; a reduction in the height is expected for a finite natural width.

The conclusions so far are completely general, independent of the specific model for inhomogeneity. We now turn to analyze several models of interacting electrons.

F. The effect of the electron-electron interaction

The effect of electron correlations on the dimerization of 1D Peierls systems was studied extensively by many groups employing various approximations for the *e-e* interaction.[38-43] The effect of the correlations on the vibrational modes of the 1D electron system such as polyacetylene has recently been studied by Horovitz and Solyom (HS) using renormalization-group methods[44] and by Baeriswyl and Maki (BM) using a variational approach[45] to solve the Peierls-Hubbard Hamiltonian.

In their renormalization-group approach HS consider the general case of *e-e* backward, forward, and umklapp scatterings with couplings g_1, g_2, and g_3, respectively. The effect of the *e-e* interaction on the gap and the renormalized phonon frequencies is expressed by a single exponent δ given in terms of the renormalized couplings g_1, g_2, and g_3. Positive δ, which is a necessary condition for dimerization, enhances the Peierls gap. Minimizing E_i yields the gap equation,

$$E_g = 2E_c[\lambda/(\lambda+\delta)]^{1/2} , \qquad (29)$$

where E_c is the cutoff energy (approximately equal to the bandwidth) and λ the *e-ph* dimensionless coupling constant. Note that for $\delta \to 0$ (i.e., no *e-e* interaction) Eq. (29) reduces to the Peierls relation Eq. (20). Considering small oscillations around the equilibrium gap, the phonon renormalization parameter $\bar{\lambda}$ [defined in Eq. (11)] is

$$\bar{\lambda} = (\lambda+\delta)/(1+\delta) . \qquad (30)$$

HS have shown also that for weak *e-e* couplings, $\delta = g_2 - 2g_1 - g_3$ and the on-site Coulomb repulsion U cancels out.

In the variational approach of BM the effect of the *e-e* interaction is contained in the on-site Coulomb repulsion U. In the limit of small U ($U < 4t$) the dimerization is enhanced and the Peierls gap increases according to the relation

$$\Delta = 2E_c \exp(-1/2\lambda_B) \qquad (31)$$

with

$$\lambda_B \simeq \lambda + 0.26(U/4t)^2 . \qquad (32)$$

Small oscillations around the equilibrium gap yield the following relation for the phonon renormalization parameter $\bar{\lambda}$:

$$\bar{\lambda}^{-1} \simeq \frac{1+0.52(U/4t)^2}{\lambda_B} - \frac{0.26(U/4t)^2}{\lambda_B^2} . \qquad (33)$$

Grabowski, Hone, and Schrieffer[43] (GHS) have studied the effect of the Coulomb interaction in an "extended Peierls Hubbard" model in which nearest neighbor, as well as on site terms, were included. Using perturbation

theory, GHS have shown that the Coulomb interaction enhances the gap for positive values of the nearest-neighbor term, V. The gap is given then by the relation

$$E_g = 4E_c \exp[-1/2(\lambda+v)] \qquad (34)$$

where $v = V/2\pi t$. Similar results were obtained by Horovitz and Krumhansl[46] (HK), who considered only the forward-scattering terms of the *e-e* Coulomb interaction. In the Hartree-Fock approximation, HK found that the gap is given by Eq. (34), where the dimensionless coupling constant v corresponds to the conventional nonretarded g_2 and g_4 couplings. We shall refer to these two models simply as the Hartree-Fock (HF) approximation. Calculating the phonon frequencies in these two equivalent models, we have found that the renormalization coupling parameter $\bar{\lambda}$ [see Eq. (11)] is given by

$$\bar{\lambda} = (\lambda+v)^2/\lambda . \qquad (35)$$

Note that in the HF approximation the on-site Coulomb repulsion cancels out, both for the gap equation and for $\bar{\lambda}$.

Inhomogeneous systems are described by a distribution $P(\bar{\lambda})$ (see the preceding section). We assume phenomenologically, that the inhomogeneity arises from a variation of some parameter (yet unspecified), which causes variations in both the *e-ph* coupling parameter λ and the *e-e* interaction parameter. The renormalization parameter $\bar{\lambda}$ will then vary according to the above relations [e.g., Eqs. (30), (33), or (35)] and will give rise to a specific $\bar{\lambda}$-Δ relation which characterizes the system. Starting from the ordered state we assume that a small change of the inhomogeneity parameter causes small changes $\Delta(\lambda) = \varepsilon$ in λ and $\Delta(e\text{-}e) = \zeta\varepsilon$ in the *e-e* coupling parameter (e.g., δ in the HS model [Eqs. (30)], $(U/4t)^2$ in the BM model [Eq. (33)], or v in the HF approximation [Eq. (35)]). Substituting these variations in the equations describing the various models [e.g., Eqs. (29)-(35)], we have found in the limit of weak disorder

$$\frac{\bar{\lambda}_0}{\bar{\lambda}} = 1 - 2\lambda c_1 \ln(\Delta/\Delta_0) - 2\lambda c_2 \ln^2(\Delta/\Delta_0)$$

$$+ O(\ln^3(\Delta/\Delta_0)) , \qquad (36)$$

where $\bar{\lambda}_0$, Δ_0, λ_0 refer to the ordered system, and c_1 and c_2 are determined by the parameters of the ordered system. In Eq. (36) the explicit dependence on ε is eliminated by incorporating it into the gap Δ, i.e., $\Delta = \Delta(\varepsilon, \zeta)$. Specific expressions for c_1 and c_2 in the various models are given in Appendix B. Note the logarithmic dependence of $\bar{\lambda}^{-1}$ on Δ implied by Eq. (36); in the absence of *e-e* interactions, the Peierls relation is obtained: $\Delta \sim \exp(-1/2\bar{\lambda})$ with $\bar{\lambda} = \lambda$, $c_1 = 1$, and $c_2 = 0$. Nonnegligible *e-e* interaction leads to $c_2 \neq 0$ and to deviations from the Peierls relation. Below we shall analyze the $\bar{\lambda}$-Δ relation for *trans*-polyacetylene and discuss the relevance of the *e-e* correlations.

G. Charge-induced infrared phonons—"phase modes"

When a charge is added to the chain the translation symmetry is lost and ir activity appears. In a multipho-

non system, the ir conductivity due to the translational or phase modes was derived in detail before[14] and is given by

$$\sigma(\omega) = i\omega \frac{e^2 \rho_c}{M_c \Omega_0^2} \frac{-D_0(\omega)}{1+(1-\alpha)D_0(\omega)} .$$ (37)

In Eq. (37), ρ_c is the average charge density, M_c is the kinetic mass of the charged defect, $\Omega_0^{-2} = \sum_n (\lambda_n/\lambda)(\omega_n^0)^{-2}$, and α is a "pinning" parameter defined by

$$\alpha = -e^2 \int dx V''(x)\rho_c(x)/(M_c N_c \Omega_0^2) ,$$ (38)

where $V(x)$ is the pinning potential for a single charge distribution $\rho_c(x)$ and N_c is the number of unit charges. The ir frequencies ω_n^ϕ are therefore solutions of

$$D_0(\omega) = -(1-\alpha)^{-1} .$$ (39)

This is identical to the equation which determines the Raman-active frequencies ω_n except that $2\tilde{\lambda}$ is replaced by α. Thus, in Fig. 4(a) a given pinning parameter defines a horizontal line and its intersection with $D_0(\omega)$ yields the IRAV frequencies. Likewise, a similar product rule holds for the ir frequencies, i.e.,

$$\prod_n \left| \frac{\omega_n^\phi}{\omega_n^0} \right|^2 = \alpha .$$ (40)

It is important to stress that the same $D_0(\omega)$, which describes the Raman amplitude modes, also determines the ir phase modes induced by the charge added either by doping ($\alpha = \alpha_{dop}$) or by photogeneration ($\alpha = \alpha_{PG}$). In trans-polyacetylene it has been found that $2\tilde{\lambda} > \alpha_{dop} > \alpha_{PG}$.

III. RRS RESULTS: AMPLITUDE MODES

A. Description of the Raman spectra

The unique feature of trans-polyacetylene samples that makes it possible to correlate the electronic gap with the phonon spectrum is the presence of a special type of inhomogeneity (or disorder), which leads to a distribution of the energy gap. This inhomogeneity is manifested by a broad interband absorption spectrum[35] as well as by the unusual dispersive RRS spectra (Fig. 1).

In this section we analyze the RRS spectrum and provide evidence for identifying the three Raman intrachain vibrations in trans-polyacetylene as amplitude modes associated with the dimerization gap. The dispersion in the Raman profiles is accounted for by a narrow distribution in the effective coupling constant $\tilde{\lambda}$.

Raman scattering from free-standing films of trans-polyacetylene, excited with two laser energies, are shown in Fig. 6 for (CD)$_x$ and in Fig. 7 for (CH)$_x$. For both isotopes there are two strongly enhanced bands, ω_1 and ω_3, and a weaker line in an intermediate Raman shift, ω_2. When excited by a red laser line ($\hbar\omega_L < 2$ eV) the lines are relatively narrow and slightly asymmetric: they are steeper on their low-frequency side. As ω_L increases, a shoulder emerges on the high-frequency side of each of the bands which gradually develops into a prominent satellite peak. Each of the Raman bands is then composed

of a nonshifting primary line and a satellite peak which shifts away from the primary as the laser photon energy increases from the red to the uv. This behavior is clearly seen for the two strong lines in Figs. 1, 6, and 7, and also for the intermediate weak line (line 2) of trans-(CH)$_x$ in the inset of Fig. 7. Three resonantly enhanced Raman lines are observed also in trans-(^{13}CH)$_x$, and show similar dispersion behavior with $\hbar\omega_L$.[1,47] We therefore conclude that trans-polyacetylene consists of three phonons which have a considerable electron-phonon coupling.[48] [A three-phonon system behavior is also seen in the IRAV spectrum of trans-polyacetylene (all isotopes) which will be discussed in Sec. IV.] To define the peak positions we deconvoluted each band into a symmetric line peaked at the primary frequency and a satellite line. The room-temperature frequencies of the primary lines $\bar\omega_n$ for each isotope are given in Table I. The straight vertical lines in Figs. 6 and 7 point at the primary (P) and at the satellite frequencies at the respective ω_L (a and b). The frequency shift $\Delta\omega_n = \omega_n - \bar\omega_n$ of each of the three satellites is plotted for (CD)$_x$ and (CD)$_x$ as a function of ω_L in Fig. 8. It is seen that $\Delta\omega_n$ (and therefore the satellite frequency itself) increases with ω_L; the primary frequencies $\bar\omega_n$ are practically independent of ω_L. Another peculiar feature of the satellite lines is the behavior of the integrated intensity I_n. Figure 9 shows I_3/I_1 for the two isotopes as a function of $\hbar\omega_L$. It is seen that the third (ω_3) satellite line monotonically increases in intensity relative to the first (ω_1) one as ω_L increases.
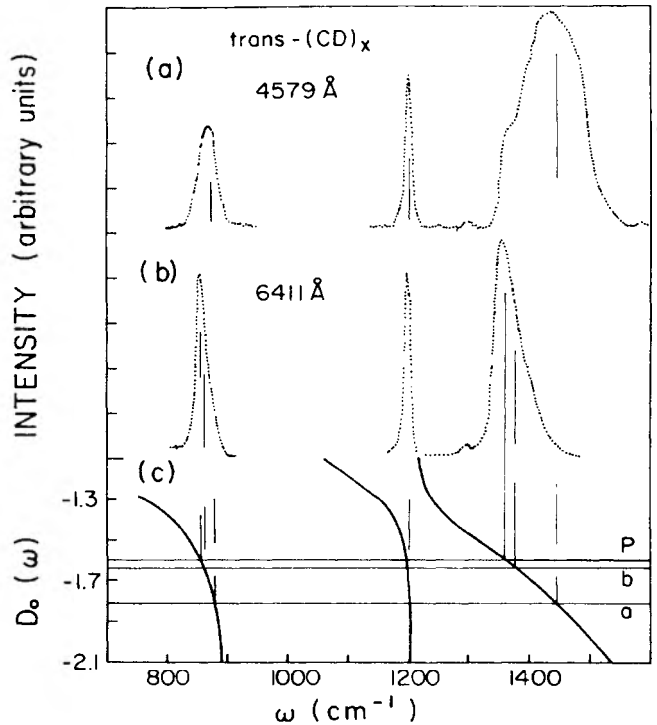

FIG. 6. RRS spectrum of trans-(CD)$_x$ at 300 K excited at (a) 2.71 eV and (b) 1.93 eV. The function $D_0(\omega)$ is shown in (c). The horizontal lines a and b correspond to the two resonance conditions and P to the primary position.

B. Analysis with the amplitude-mode model

The Raman data provide clear evidence that the inhomogeneity can be expressed as a distribution in the renormalization coupling parameter $\tilde{\lambda}$ [Eq. (11)]. The product-rule relation [Eq. (12)] shows that the upward shift of *all* satellite frequencies with ω_L infers a dependence of $\tilde{\lambda}$ on $\hbar\omega_L$. Defining ω_n^* and $\tilde{\lambda}^*$ as the satellite frequency and $\tilde{\lambda}$ at some reference laser energy $\hbar\omega_L^*$, we obtain from Eq. (12) the following product rule based on experimentally measured frequencies alone:

$$\prod_{n=1}^{3}\left|\frac{\omega_n^*}{\omega_n}\right|^2=\frac{\tilde{\lambda}^*}{\tilde{\lambda}}, \tag{41}$$

where ω_n are the satellite frequencies. In deriving Eq. (41), we have assumed that the bare frequencies ω_n^0 are fixed and independent of the disorder. Figure 10 shows the product (41) for both $(CH)_x$ and $(CD)_x$ as a function of $\ln(\hbar\omega_L)$ for ten different laser photon energies in the range 1.9–3.5 eV for $\hbar\omega_L^*=2.6$ eV. It is seen first that the product (or the ratio $\tilde{\lambda}^*/\tilde{\lambda}$) is nearly independent of the isotope, although the satellite frequencies themselves differ substantially for these two isotopes. This is an experimental indication that $\tilde{\lambda}$ is not a pure "phononic" quantity but indeed originates from an electronic term in
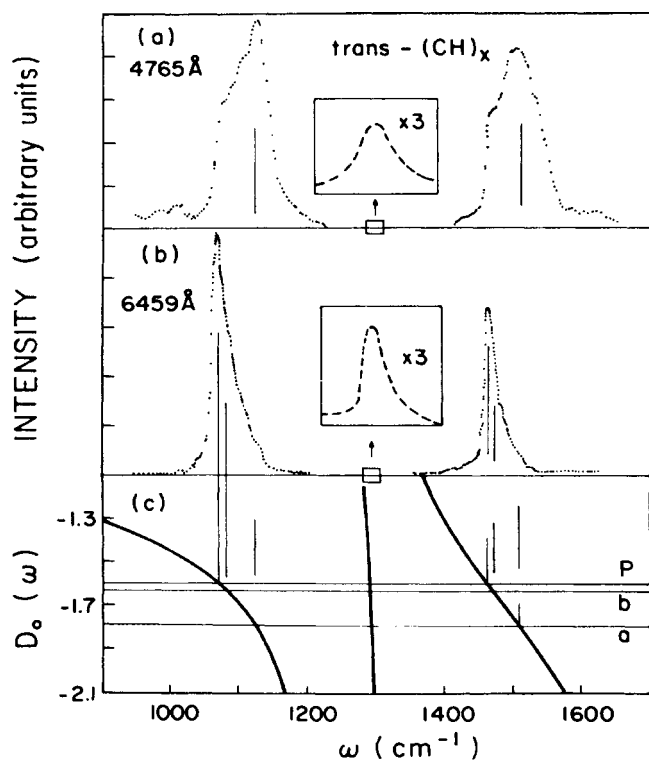
the Hamiltonian as implied by Eq. (11). Secondly, the straight solid line through the data points in Fig. 10 infers a linear dependence of $\tilde{\lambda}^{-1}$ on $\ln(\hbar\omega_L)$. A least-square fit of the data to a linear dependence gave the following relation between $\tilde{\lambda}$ and $\ln(\hbar\omega L)$:

$$(2\tilde{\lambda})^{-1}=B^*[\ln(4A)-\ln(\hbar\omega_L)] \tag{42}$$

with $A=6.3\pm0.3$ eV, $B^*=(0.44\pm0.01)/2\tilde{\lambda}^*$, and $\hbar\omega_L$ is expressed in eV. Note that $\tilde{\lambda}^*$ cannot be determined from this plot. The resonance condition $\hbar\omega_L=E_g$ implies an increase of the gap with $\tilde{\lambda}$ in a manner similar to the Peierls relation [Eq. (20)], identifying thus $\tilde{\lambda}$ with the e-ph coupling constant λ. However, in deference to Eq. (36) which gives the $\tilde{\lambda}$-Δ relation when the Coulomb correlations are included, we have fitted the data presented in Fig. 10 by including also a $\ln^2(\hbar\omega_L)$ term. We have found that the coefficient of this term is small; in the notation of Eq. (36), $c_2/c_1<0.1$. In spite of the small deviation from a Peierls-type relation, we shall see below that the Coulomb interaction should not be neglected.

To actually fit the data, obtained from the 10 laser energies shown in Figs. 8 and 9 to Eq. (9) (30 equations for a three-line spectrum at 10 laser energies), we used the following parameters: the three bare frequencies $(\omega_n^0$, $n=1,2,3)$ and two independent couplings $(\lambda_n/\lambda$,

FIG. 7. RRS spectrum of *trans-*$(CH)_x$ at 300 K excited at (a) 2.60 eV and (b) 1.92 eV. The insets are blown up scales of line 2, showing the change in shape with ω_L. The function $D_0(\omega)$ is shown in (c). The horizontal lines a and b correspond to the two resonance conditions and P to the primary position.
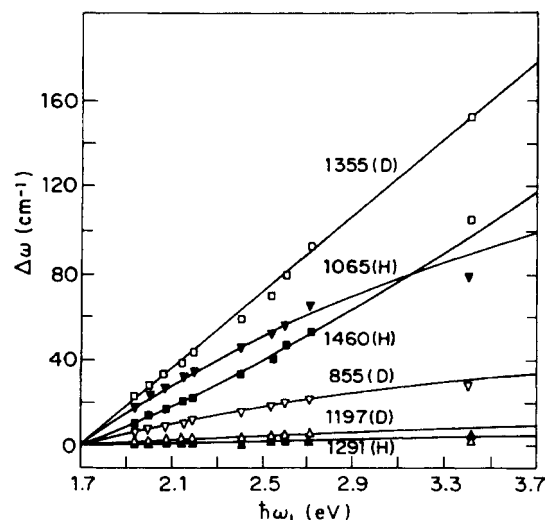

FIG. 8. The dependence of the satellite shifts $(\Delta\omega_n)$ on the laser energy $(\hbar\omega_L)$ for *trans-*$(CH)_x$ (open symbols) and *trans-*$(CD)_x$ (solid symbols). The solid lines are theoretical.

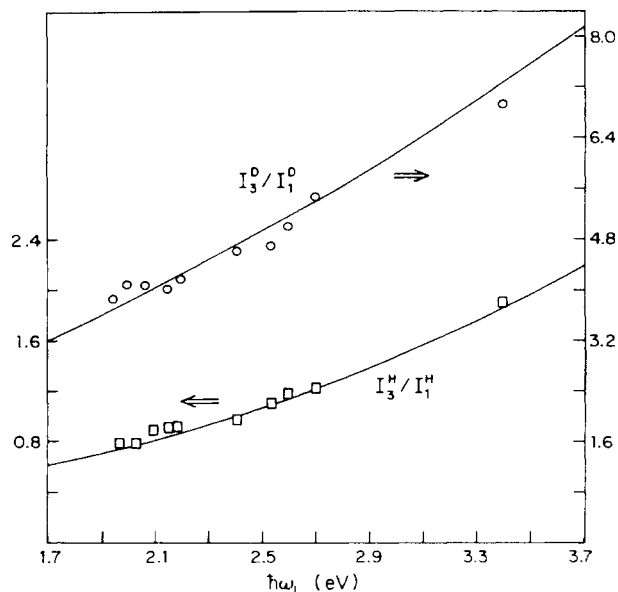FIG. 9. The intensity ratio I_3/I_1 vs $\hbar\omega_L$ for trans-(CH)$_x$ and (CD)$_x$. The solid lines are calculated using Eq. (25).

$n = 1,2,3$, $\sum_n \lambda_n = \lambda$) of the function $D_0(\omega)$ and the 10 values of $\bar{\lambda}$ at each of the 10 laser energies. Utilizing the product rule [Eq. (12) or (41), for each laser energy], we reduce the parameter space by a factor of 3 from 15 to 5 while reducing the number of the independent equations from 30 to 20 only. The parameters of $D_0(\omega)$ obtained in this way are given in Table II for (CH)$_x$ and (CD)$_x$. Also given in Table II for comparison are the parameters for trans-(^{13}C H)$_x$ that we have determined elsewhere.[47] Us-
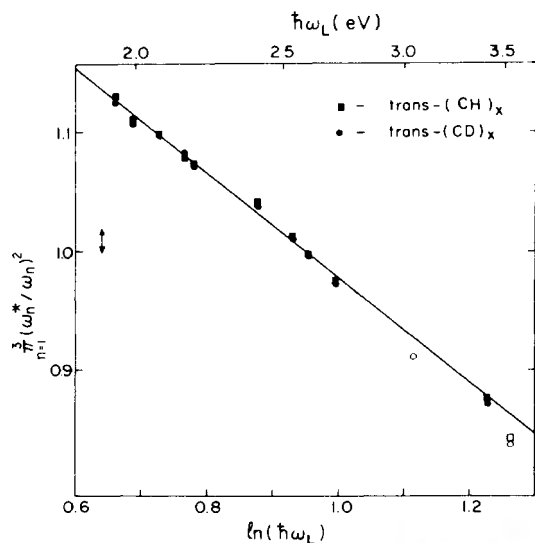

FIG. 10. The experimental relation $\prod_{n=1}^{3}(\omega_n^*/\omega_n)^2$ vs $\ln(\hbar\omega_L)$ for trans-(CH)$_x$ and (CD)$_x$ at 300 K. The * corresponds to the data at $\hbar\omega_L^* = 2.6$ eV. The straight line is a linear fit through the data points. Data at $\hbar\omega_L = 3.05$ eV (Ref. 4) and 3.53 eV (Ref. 1) are shown as open symbols.

ing now the product-rule relation [Eq. (12)] we can determine $\bar{\lambda}$ from the RRS spectrum, for each laser excitation energy. In particular, for $\hbar\omega_L^* = 2.6$ eV we have found $2\bar{\lambda}^* = 0.44 \pm 0.01$; thus in Eq. (42), $B^* = 1.00 \pm 0.04$ for both trans-(CH)$_x$ and (CD)$_x$. Thus Eq. (42) expresses a special type of inhomogeneity, and we shall discuss below how to describe it by a disorder mechanism which affects both the e-ph and e-e interactions.

The calculated $D_0(\omega)$ for each isotope is plotted in Figs. 6 and 7 showing the way in which the satellite frequencies ω_n increase with ω_L. At higher ω_L, resonance conditions are matched by larger E_g (and $2\bar{\lambda}$) so that the horizontal lines drawn at $-(1-2\bar{\lambda})^{-1}$ intersect $D_0(\omega)$ at higher frequencies. In this way we obtained the curves of the satellite line shifts $\Delta\omega_n$ versus $\hbar\omega_L$ for the six phonons of trans-(CH)$_x$ and trans-(CD)$_x$ in Fig. 8. It is seen that the above solution for $D_0(\omega)$ indeed yields a remarkably good agreement with the experimental $\Delta\omega_n$. In addition, using Eq. (25) for the line intensity, we obtained the relative intensity curves shown in Fig. 9; again the agreement is remarkably good. Note that the intensities $I_n(\omega_L)$ were not included in our fitting process, so that the good agreement is not obvious as for $\omega_n(\omega_L)$. As discussed above, not only I_n is inversely proportional to $D_0'(\omega)$, but also the satellite shifts $\Delta\omega_n$ and the Raman linewidth $\delta\omega_n$ (in the case of small natural width) also are. This can be clearly seen, for instance, in Fig. 6 for (CD)$_x$ where $D_0'(\omega_2)$ is the highest and $\Delta\omega_2$, I_2, and $\delta\omega_2$ are the smallest; also for (CH)$_x$ $I_1 > I_2 > I_3$ (for $\hbar\omega_L = 2$ eV), while the order is reversed in $D_0'(\omega_n)$.

We have thus clearly shown in this section that the AM theory accounts for the frequency shift of all three lines in all isotopes and for the relative intensities of the two strong RRS lines as ω_L is varied. We have also determined the $\bar{\lambda}$-Δ relation characteristic of the inhomogeneity in trans-polyacetylene.

C. The distribution function

The good agreement obtained so far shows that the satellite frequencies are solutions of $D_0(\omega) = -(1-2\bar{\lambda})^{-1}$ at different $\bar{\lambda}$ values. The system can therefore be characterized by a distribution $P(\bar{\lambda})$ of the renormalization coupling parameter $\bar{\lambda}$. The Raman cross section is thus given by the expression for an inhomogeneous system, Eq. (26). We note again that since the quasi-one-dimensional matrix elements function f [Eqs. (23) and (24) and Fig. 5] has a sharp and strong peak at resonance, $\hbar\omega_L = E_g$, the cross section [Eq. (26)] is double peaked corresponding to Raman frequencies which are determined by Eq. (9) with different values of $\bar{\lambda}$: the primary line at the maximum of $P(\bar{\lambda})$ and the satellite at the $\bar{\lambda}$ of the resonance given by $E_g(\bar{\lambda}) = \hbar\omega_L$. We emphasize that a single-peak distribution is sufficient to account for a double-peak Raman structure. The fact that for each phonon there is only one "primary" line, which does not shift with $\hbar\omega_L$, strongly indicates a single-peak distribution $P(\bar{\lambda})$, contrary to previous suggestions.[6,9,10] Using the primary frequencies of Table I and the product-rule relation, we find that $P(\bar{\lambda})$ peaks at $2\bar{\lambda}_0 = 0.371 \pm 0.005$ for (CH)$_x$ and at 0.375 ± 0.005 for (CD)$_x$ at 300 K. The corresponding

TABLE II. The parameters of $D_0(\omega)$ for *trans*-polyacetylene isotopes at 300 K. ω_n^0 are given in 10^3 cm^{-1}.

trans-(CH)$_x$		*trans*-(CD)$_x$		*trans*-(^{13}CH)$_x$	
ω_n^0	$\lambda_{n/\lambda}$	ω_n^0	$\lambda_{n/\lambda}$	ω_n^0	$\lambda_{n/\lambda}$
1.23	0.07	0.92	0.06	1.22	0.05
1.31	0.02	1.21	0.005	1.29	0.05
2.04	0.91	2.04	0.93	1.96	0.90

one-dimensional gaps can be obtained from Eq. (42) with $B^* = 1.0$ (see Sec. III B). We find $2\Delta = 1.7 \pm 0.1$ eV for both *trans*-(CH)$_x$ and *trans*-(CD)$_x$ at 300 K. An upper limit estimate of the width of $P(\tilde{\lambda})$ can be obtained from the width of the lines recorded at red excitation where the resonance appears near the peak of $P(\tilde{\lambda})$. Although the functional dependence of $P(\tilde{\lambda})$ away from its mean value cannot be determined without extensive fittings, the fact that the absolute cross section of the satellite does not diminish very rapidly as ω_L increases towards the uv means that $P(\tilde{\lambda})$ falls relatively slowly for $\tilde{\lambda} > \tilde{\lambda}_0$.

The shape of $P(\tilde{\lambda})$ can be estimated using Eq. (28). When the broadening of the Raman line due to the phonon natural width is small, the RRS cross section is proportional to $|f|^2 P(\tilde{\lambda})/E_g^2$. The gap $E_g(\tilde{\lambda})$ has been determined experimentally and is given by Eq. (40). The function f is assumed to have the 1D Peierls form, as in Eqs. (23) and (24). However, in order to obtain reliable results for $P(\tilde{\lambda})$ we have analyzed spectra showing clearly both primary and satellite structure ($\hbar\omega_L > 2.6$ eV) such that the deduced $P(\tilde{\lambda})$ is practically insensitive to the detailed shape of f at resonance. Thus, by dividing the RRS cross section by $|f|^2/E_g^2$, we obtain the derived distribution function $P(\tilde{\lambda})$ shown in Fig. 11. Figure 11(a) shows the function $P(\tilde{\lambda})$ derived from lines 1 and 3 of the *trans*-(CH)$_x$ spectrum shown in Fig. 7(a). Both lines yielded almost identical distribution functions (as they should) peaked at $2\tilde{\lambda} = 0.371$. The low cutoff at $2\tilde{\lambda} = 0.36$ is determined by the finite background of the experimental data. Note that although the experimental spectrum shows only a shoulder at the primary frequency the derived $P(\tilde{\lambda})$ has a definite peak at $\tilde{\lambda} = \tilde{\lambda}_0$. Figure 11(b) shows the derived $P(\tilde{\lambda})$ as obtained for *trans*-(CD)$_x$ from the spectrum shown in Fig. 6(a). The distribution function derived from line 3 of trans-(CD)$_x$ is similar in shape to that obtained for *trans*-(CH)$_x$. On the other hand, the shape (below $2\tilde{\lambda} \sim 0.38$) of the distribution derived from line 1 is probably unreliable since line 1 in trans-(CD)$_x$ is narrow, and Eq. (28) may not be applicable to this line.

This method of deriving $P(\tilde{\lambda})$ is thus suitable for samples with significant amount of disorder so that the natural width can be neglected, but may not be applicable to samples where the width due to the disorder is small. We note, however, that inspection of the curves shown in Fig. 11 shows that they follow very nearly a Lorentzian shape function in the range $2\tilde{\lambda} \sim 0.36$ to $2\tilde{\lambda} \sim 0.41$. Thus, in order to obtain an estimate of the width of $P(\tilde{\lambda})$ in "good" samples with narrow features which show explicitly double-peak structure we tried to fit the Raman spectrum by taking a Lorentzian-shape function for $P(\tilde{\lambda})$. Since the

heights of the various Raman lines are not equal it is necessary to take into account the finite natural width of the bare phonon modes. The actual fit has been done by taking the following free parameters: (a) the natural width δ_n of the three bare phonon modes, (b) the mean value $2\tilde{\lambda}_0$ and the half width at half maximum Γ (in units of $2\tilde{\lambda}$) for the Lorentzian shaped $P(\tilde{\lambda})$, and (c) the 3D cutoff W_1 of the matrix-element function $f(\hbar\omega_L/E_g)$ and the height of $f(x)$ at resonance, $x = 1$. An example of our fit for a good sample is shown in Fig. 12 as a solid line through the data points. It is clearly seen that the Lorentzian-shape function duplicates the double-peak structure and gives an overall good fit. We note here that the fits shown in Fig. 12 are not sensitive to the actual shape of $P(\tilde{\lambda})$ below $2\tilde{\lambda} < 0.355$ ($E_g < 1.5$ eV). Thus no information is obtained here about the low-energy side (below about 1.5 eV) of the distribution. The parameters needed for the fit shown in Fig. 12 and those needed for
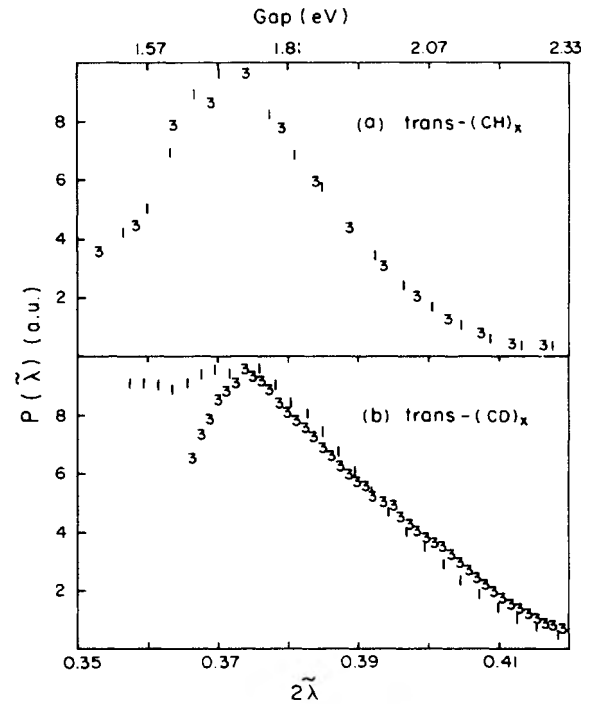

FIG. 11. The distribution function $P(\tilde{\lambda})$ vs $2\tilde{\lambda}$ for (a) *trans*-(CH)$_x$ and (b) *trans*-(CD)$_x$ derived [using Eq. (28)] from the data of Figs. 6(a) and 7(a) for lines 1 and 3. The upper scale translates $2\tilde{\lambda}$ to the energy domain assuming the experimental relation Eq. (42).
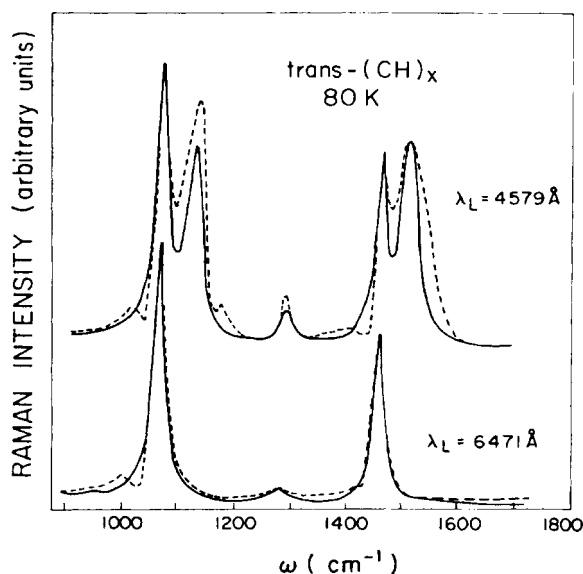
FIG. 12. RRS spectra of trans-$(CH)_x$ sample with well-separated double-peak structure. Dashed line, experimental data of Ref. 6. Solid line, theoretical fit with the parameters of Table III.

temperature-dependent energy gap in trans-polyacetylene, in agreement with other experiments.[49]

The effects of the natural bare phonon width on the height of the RRS lines are apparent in Fig. 1: When the uv spectrum is compared with that of the red, it is seen that the heights of lines 1 and 2 are small compared with line 3. This is readily explained by the following property of $D_0(\omega)$ (Figs. 6 and 7): as ω_L increases towards the uv (higher $\bar{\lambda}$) the slope of $D_0(\omega)$ at the positions of lines 1 and 2 increases much faster than that of line 3. As a result, a given width of $P(\bar{\lambda})$ causes smaller broadening of lines 1 and 2 and their natural width becomes more effective in the broadening mechanism and in the reduction of the height for the uv excitation.

D. The Raman excitation profile

The Raman excitation profiles were studied previously by several groups. It was found experimentally that (a) the absolute cross section of each RRS band is peaked roughly at the absorption maximum, but it is considerably narrower than the interband absorption band;[50,51] and (b) the "sliced excitation profile," where the RRS intensity at a fixed Raman frequency is measured as a function of ω_L, shows generally a reduction as $\hbar\omega_L$ increases from 1.8 to 2.7 eV.[10,50] The reduction is the strongest for the primary frequencies [1070 cm^{-1} for line 1 or as it is commonly called the "C—C band" and 1460 cm^{-1} for line 3 or the "C$=$C band" of trans-$(CH)_x$]. As the selected vibrational frequency is increased, the measured cross sections decrease in intensity and their dependence on $\hbar\omega_L$ weakens (Fig. 13). These two features can be understood within our model in the following way. Both the optical absorption and the RRS cross section depends upon the density of states of the π electrons, but in a different way. The optical absorption is proportional to the joint density of states[35] which is peaked at E_g in quasi-one-dimension and falls off as $(E - E_g)^{-1/2}$ for $E > E_g$. The RRS cross section is given by the function $|f|^2$ which also peaks at $\hbar\omega_L = E_g$ but falls off as $(\hbar\omega_L - E_g)^{-3}$, i.e., much more rapidly than the joint density of states. Thus the RRS excitation profile is narrower than the absorption spectrum. For comparison, we show in Fig. 14 the calculated RRS cross section and the interband absorption. In Fig. 14 we utilize the distribution function $P(\bar{\lambda})$ given in Fig. 11, and assume 1D Peierls chains with 3D cutoff energy given in Table III. It is seen that the RRS cross-section profile is

the fit of the Raman spectra of other samples are given in Table III. Two remarks are in order while assessing these parameters: (a) Since the relative intensity of the weakly coupled intermediate line (line 2) is not obtained accurately by the AM model (see above), their linewidth has been chosen to give a representative fit to the experiment. Thus we believe that the actual natural linewidth of line 2 in trans-$(CH)_x$ is smaller than the value given in Table III, whereas that of trans-$(CD)_x$ is larger. (b) Since the 3D cutoff energy $W_\perp$ should be an intrinsic property of the trans-polyacetylene structure we have kept it the same for all samples. Its value of $W_\perp \sim 0.3$ eV is within the range of theoretical estimates.[35—37] The main result which emerges from these fits is the sample dependency of the width Γ of $P(\bar{\lambda})$: good samples which show clear double-peak structure have smaller Γ than those in which the lines are smeared. We therefore conclude that the samples of trans-polyacetylene differ mainly in the width of the distribution function describing their inhomogeneity. Note also that the value of $2\bar{\lambda}_0$ is slightly isotope and temperature dependent, which indicates weak isotope and

TABLE III. Fitting parameters for RRS spectrum of several samples of trans-polyacetylene. See remarks in text for the values of δ_2 and $W_\perp$.

| | Natural width (cm^{-1}) | | | $P(\bar{\lambda})$ | | 3D cutoff |
	δ_1	δ_2	δ_3	$2\bar{\lambda}_0$	Γ	$W_\perp$ (eV)
$(CH)_x$[a]	20	15	20	0.371	0.015	0.3
$(CD)_x$[b]	20	2	20	0.375	0.015	0.3
$(CH)_x$[c]	20	15	20	0.365	0.005	0.3
$(^{13}CH)_x$[d]				0.380		

[a]Figure 7, 300 K.
[b]Figure 6, 300 K.
[c]Reference 4, 80 K.
[d]References 1 and 46, 300 K.

indeed narrower than the absorption spectrum. The calculated sliced excitation profile is compared with the experimental data in Fig. 13 (solid line); the agreement is satisfactory, showing indeed that the RRS intensity decreases as $\hbar\omega_L$ increases from 1.8 to 2.5 eV.

IV. PHOTOINDUCED ABSORPTION IN THE ir REGIME—PHASE MODES

A. Analysis of the IRAV spectra

IRAV are phase modes whose frequencies and line shape can be derived from the same $D_0(\omega)$ that describes the Raman data. The IRAV frequencies are determined by a pinning parameter α [Eq. (39)] instead of $\tilde{\lambda}$ in the case of the Raman data. There is no direct relation between α and $\tilde{\lambda}$ since the incommensurate charge density is pinned by random potentials arising from the dopant ions or impurities which are thus a plausible source for the distribution in the values of the pinning parameter α. It is necessary therefore to determine α and its distribution from the observed spectrum. Figure 2 shows the IRAV spectra of doping and photogeneration (PG) in *trans*-$(CD)_x$. The measured ir frequencies together with the predetermined $D_0(\omega)$ (see Table II) yield a weak pinning of $\alpha=0.06$ for PG and a much stronger pinning of $\alpha=0.23$ for the 1% doping. The comparison between the measured IRAV frequencies and relative intensities and those predicted are given in Tables IV and V for all three isotopes.

The very large width of the low-frequency IRAV line ("the pinning mode") in both doping and PG (Fig. 2) implies the presence of a distribution $P(\alpha)$ of the pinning parameter α. In this case the ir absorption spectrum is obtained by integrating Eq. (37) over α,
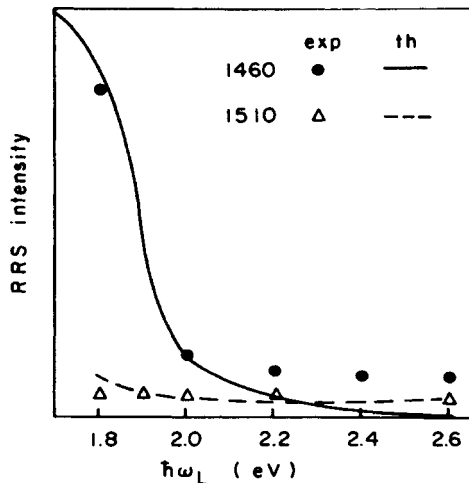

FIG. 13. Sliced excitation profile for line 3 of *trans*-$(CH)_x$. Experimental points are from Ref. 50; calculated curves are with the parameters of Tables II and III.
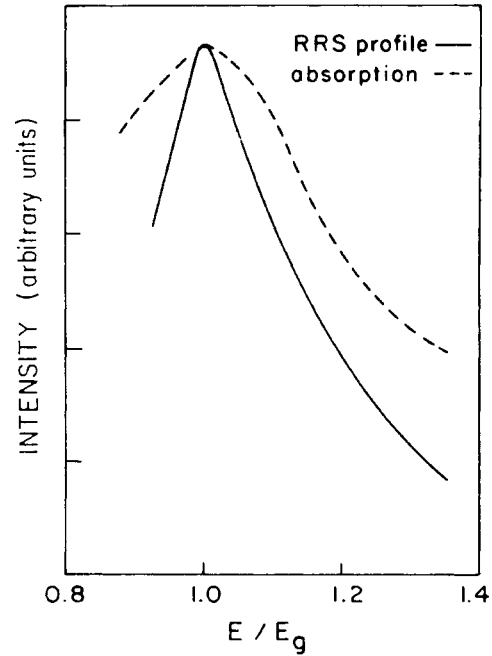

FIG. 14. Calculated RRS profile and interband absorption for *trans*-$(CH)_x$ at 300 K using the parameters of Tables II and III.

$$\sigma_A(\omega) = \int d\alpha\, P(\alpha)\mathrm{Re}\sigma(\omega)$$
$$= \frac{\omega e^2 \rho_c}{M_c \Omega_0^2} \int d\alpha\, P(\alpha)\mathrm{Im}\left|\frac{-D_0(\omega)}{1+(1-\alpha)D_0(\omega)}\right| . \tag{43}$$

The absorption σ_A, like the Raman cross section [Eq. (28)], takes a very simple form when the natural bare phonon widths are small, i.e.,

$$\sigma_A(\omega) \propto \omega P(\alpha_\omega) , \tag{44}$$

where α_ω satisfies $\alpha_\omega = 1 + D_0^{-1}(\omega)$. Equation (44) enables us to experimentally derive the distribution $P(\alpha)$ from the measured IRAV line shapes by plotting σ_A/ω versus $\alpha_\omega = 1 + D_0^{-1}(\omega)$. Figure 15 shows the result of such plots of doping and PG IRAV, for *trans*-$(CD)_x$. It is seen that the distribution functions peak at $\alpha \sim 0.06$ for PG and at $\alpha \sim 0.23$ for doping-induced IRAV, while the half width at half maximum is $\Gamma \sim 0.03$ for PG and $\Gamma \sim 0.1$ for doping; similar results were obtained also for $(CH)_x$.

B. Determination of the soliton defect mass

The amplitude-mode formalism provides a unique way to directly determine the mass of the soliton defect in *trans*-polyacetylene from the photoinduced absorption (PA) experimental spectrum. The signal in PA arises from the changes in the optical-absorption constant due to the presence of photoexcited carriers. The PA spectrum in *trans*-polyacetylene is composed of vibrations (IRAV modes; see above) and electronic transitions as shown in Fig. 16 for the two isotopes $(CH)_x$ and $(CD)_x$. The PA

TABLE IV. Induced ir active phonon frequencies (in cm^{-1}) in polyacetylene by doping and photo-generation. T denotes theoretical, E denotes experimental.

| | | $\alpha = 0.23$ ir doping | | $\alpha = 0.06$ ir photogeneration | |
		T	E	T	E
$(CH)_x$	1	886	888	488	500
	2	1285	1288	1278	1275
	3	1397	1397	1364	1365
$(CD)_x$	1	770	790	410	400
	2	1148	1140	1045	1045
	3	1236	1240	1216	1224
$(^{13}CH)_x$	1	844	821	465	
	2	1251	1250	1247	
	3	1385	1382	1359	

spectrum contains also an absorption band at 1.4 eV,[52] which is due to neutral photoexcitation,[53] and thus does not produce any IRAV. The low-energy (LE) band which peaks at 0.43 eV (Fig. 16) is due to charged solitons[21,54] on the chains and therefore the photoinduced IRAV are intimately related[14] to this electronic transition. Since the photoinduced IRAV and LE band are measured simultaneously with the same setup, it is possible to compare their absorption strength in the PA spectrum in order to determine the soliton mass.

The sum of the three IRAV absorption intensities $I_v = \sum_n I_n$ is related to the soliton mass via the equation[14,55]

$$I_v = \sum_{n=1}^{3} I_n = \frac{\rho_c \pi e^2}{2M_s} \frac{\Omega_1^2}{\Omega_0^2} , \qquad (45)$$

where ρ_c is the photoinduced charge density and ω_n are normalized phonon frequencies[14]

$$\Omega_0^{-2} = \sum_n (\lambda_n/\lambda)(\omega_n^0)^{-2}, \quad \Omega_1^2 = \sum_n (\lambda_n/\lambda)(\omega_n^0)^2 .$$

These parameters can be readily calculated from the parameters of $D_0(\omega)$ given in Table I.

In Eq. (45), I_v is a measured quantity. However, since our experimental setup is limited to frequencies higher than ~ 720 cm^{-1}, we are unable to record the lowest IRAV line (the "pinning mode").[14] This experimental difficulty can be easily overcome by calculations involving

again the $D_0(\omega)$ function. The contribution of each individual IRAV intensity to the sum rule $W_n = I_n/I_v$ is proportional to $\omega_n/D_0'(\omega_n)$ (Refs. 14 and 55). Since $D_0(\omega)$ and α for photogeneration are known, we can calculate the contributions of the three IRAV modes and thus obtain W_n. Therefore the experimental determination of a single IRAV, I_n, is sufficient to determine I_v ($I_v = I_n/W_n$).

The soliton "midgap" integrated intensity I_s within the Peierls model is given by[56]

$$I_s = 2.8\rho_c e^2/m^* , \qquad (46)$$

where m^* is the band effective mass $m^* = 0.1m_e$ (Ref. 36) and m_e is the electron mass. Dividing Eqs. (46) by Eq. (45), ρ_c is eliminated and M_s is given by

$$M_s = \frac{\pi I_s \Omega_1^2}{5.6 I_v \Omega_0^2} , \qquad (47)$$

where I_s/I_v is derived from the PA spectrum; I_s is the integrated intensity of the LE PA band and I_v is the integrated intensity of the PA IRAV.

From Fig. 16 we have measured $I_s^H/I_3^H(1360$ cm$^{-1}) \sim 90$ for $trans$-$(CH)_x$, whereas for $trans$-$(CD)_x$ $I_s^D/I_2^D(1045$ cm$^{-1}) \sim 35$. We have chosen the strongest IRAV mode for each isotope to determine I_v more accurately. From $D_0(\omega)$ of each isotope we calculate $W_3(1360$ cm$^{-1}) = 0.15$ for $(CH)_x$ and $W_2(1045$ cm$^{-1}) = 0.39$ for

TABLE V. Intensity ratio for IRAV induced by doping or photogeneration and for RRS at $\hbar\omega_L = 2$ eV in three $trans$-polyacetylene isotopes. T denotes theoretical, E denotes experimental.

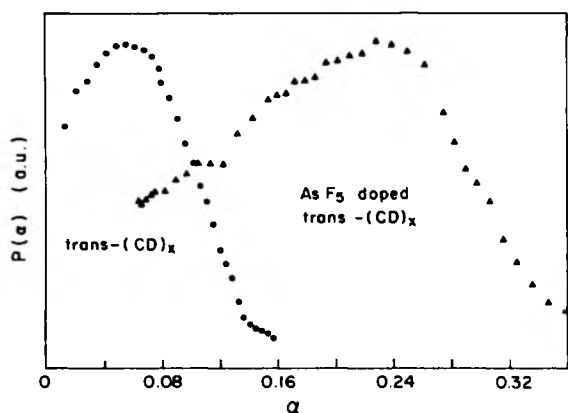| | I_3/I_1 ir doping | | I_3/I_2 ir doping | | I_3/I_2 ir photogeneration | | I_3/I_2 RRS | |
	E	T	E	T	E	T	E	T
$(CH)_x$	0.25	0.28	10	9.5	4	5	100	16
$(CD)_x$	0.9	0.6	0.4	0.5	0.07	0.09	6	16
$(^{13}CH)_x$	0.25	0.23	11	9.5		7	30	11

FIG. 15. The derived distribution functions for the pinning parameter of the induced charged carriers (doping and PG) as obtained from the IRAV spectra of *trans-*(CD)$_x$.

$(CD)_x$. Therefore, the PA experiment gives $I_s^H/I_v^H = 13.5$ for $(CH)_x$ and $I_s^D/I_v^D = 13.7$ for $(CD)_x$. The close values for I_s/I_v for the two isotopes justifies the method used to determine this ratio. The remaining unknowns in Eq. (45) can be readily calculated from the parameters of $D_0(\omega)$ (Table II). We have calculated $\Omega_0 = 1900$ cm^{-1}, $\Omega_1 = 1980$ cm^{-1}, and $(\pi/2)\Omega_1^2/\Omega_0^2 = 1.71$ for $(CH)_x$, while for $(CD)_x$ we have found $\Omega_0 = 1822$ cm^{-1}, $\Omega_1 = 1988$ cm^{-1}, and $(\pi/2)\Omega_1^2/\Omega_0^2 = 1.87$. Substituting these in Eq. (45), we have calculated for the two isotopes $M_s((CH)_x) = 0.82m_e$ and $M_s((CD)_x) = 0.91m_e$; note that $M_s((CD)_x) > M_s((CH)_x)$ as it should. These masses deviate somewhat from the predicted soliton mass of $3m_e$ (Refs. 23 and 56); the deviation is due either to the uncertainties of the parameters or the role of Coulomb interactions. Note that if the total interband transition intensity were available a conductivity sum rule[14] could be used instead of I_s and the uncertainties due to Coulomb interactions would be eliminated.
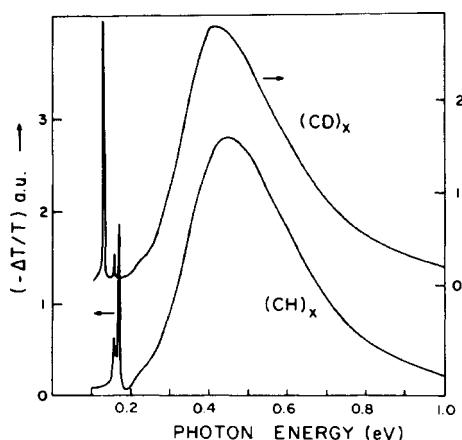

FIG. 16. The photoinduced absorption spectrum of *trans-*(CH)$_x$ and (CD)$_x$ up to 1 eV showing the IRAV modes and the charge-induced absorption bands.

V. DISCUSSION

A. Electron correlations in trans-polyacetylene

The experimental $\tilde{\lambda}$-Δ relation found in *trans-*polyacetylene (see Sec. III B) provides us with the possibility to estimate the *e-e* interaction parameters.

Identifying the primary lines (see for instance Fig. 1) with the ordered state, we obtain using Tables I and II,

$$2\tilde{\lambda}_0 = \prod_{n=1}^{3} (\omega_n/\omega_n^0)^2 = 0.37 \pm 0.01$$

for both *trans-*(CH)$_x$ and *trans-*(CD)$_x$. The data presented in Fig. 10 can then be expressed by Eq. (36) with $2\lambda_0 c_1 = 0.37$ and $c_2/c_1 < 0.1$. Using the corresponding expressions for c_1, c_2, and $\tilde{\lambda}$ for the three models presented in Sec. II F [e.g., Eqs. (B1), (B2), and (30) for the renormalization-group method of Horovitz and Solyom[44]], we have calculated ranges of possible values for the *e*-ph and *e-e* coupling parameters. These ranges are shown diagrammatically in Fig. 17 for two of the models, namely, the renormalization-group method[44] and the Hartree-Fock (HF) approximation.[43,46] The solid lines give the possible values of the pair δ_0, λ_0 [Fig. 17(a)] or v_0, λ_0 [Fig. 17(b)] that are compatible with the data of
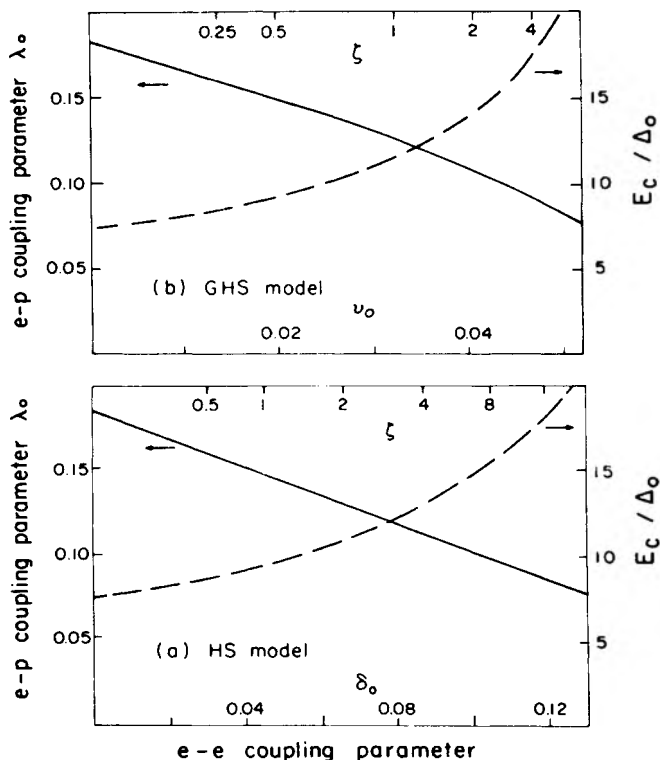

FIG. 17. Diagram of possible values of the *e*-ph and *e-e* dimensionless coupling parameters for *trans-*(CH)$_x$. Solid lines, possible values of the pairs (a) (λ_0, δ_0) for the HS model (Ref. 44) or (b) (λ_0, v_0) for the Hartree-Fock approximation (Refs. 43 and 46). Dashed lines, the corresponding values for E_c/Δ_0. The upper scale indicates the corresponding values of the parameter ζ (see text).

Fig. 10, with $2\bar{\lambda}_0=0.37$ and with Eq. (36) (i.e., with $c_2/c_1<0.1$ which determines the range of δ_0 or ν_0 in Fig. 17). The upper scale gives the relative sensitivity of the e-ph and e-e couplings to disorder; for instance, $\zeta=0$ corresponds to inhomogeneity due only to variation in λ whereas $\xi=\infty$ corresponds to variation in the e-e coupling parameter alone. The parameter ζ is defined in Sec. II F. The dashed lines give the possible values for E_c/Δ_0 taken from Eq. (29) for the HS model[44] [Fig. 17(a)] or Eq. (34) for the HF approximation[43,46] [Fig. 17(b)]. The left-hand-side axis in Fig. 17(a) corresponds to the Peierls model [i.e., no Coulomb interaction ($\delta_0=0$), and a distribution in the e-ph coupling parameter only ($\zeta=0$)] for which we find $\lambda_0=0.185$ and $E_c/\Delta_0=7.4$. With our value of $2\Delta_0\sim1.7$ eV at 300 K we obtain for the π-π^* bandwidth $E_c=6.3$ eV which is lower than most estimates. In the presence of e-e correlations Fig. 17 yields *smaller* e-ph coupling λ_0 and a finite e-e interaction parameter. The exact values cannot be determined unless an additional assumption is made. If we assume, for instance, that the π-π^* bandwidth is $E_c=4t=10$ eV (Refs. 36 and 37), we find for the HS model[44] [Fig. 17(a)], $\lambda_0=0.12$ and $\delta_0=0.08$ with the corresponding value of $\zeta\sim3$. These values imply finite (though small) e-e interaction strength and an inhomogeneity mechanism in which the variation in the e-e coupling parameter is relatively important ($\zeta\sim3$). Likewise, we have found from Fig. 17(b) for the HF approximation: $\lambda_0=0.13$, $\nu_0=V_0/2\pi t=0.025$, and $\zeta\sim0.5$. The value of ν_0 yields for the nearest-neighbor Coulomb interaction $V_0=0.4$ eV, which is in rough agreement with the GHS (Ref. 43) estimate. Similarly, the Peierls-Hubbard model[45] yields $\lambda_0=0.12$ and $U/4t=0.37$ or $U=3.7$ eV for the on-site Coulomb interaction.

We have thus shown that the $\bar{\lambda}$-Δ plot (Fig. 10) gives a reasonable range of values for the e-e interaction parameters which are compatible with the experimental Peierls-like relation and with theoretical estimates. We have also shown that the inhomogeneity mechanism may affect *both* the e-ph and the e-e interactions.

B. The σ-bond force constant

The high-frequency Raman mode (line 3) has long been associated with the carbon-carbon stretching mode of the *trans*-polyacetylene chain. Yet by replacing H with D line 3 shifts by ~100 cm^{-1}, nearly as much as line 1 or 2 (see Table I). Furthermore, the frequencies of Table I seem to indicate that none of the modes is a pure carbon-carbon stretch. However, realizing that the observed Raman frequencies are determined via $D_0(\omega)$ from Eq. (9), we should consider the changes occurring in the *bare* phonon frequencies by replacing the isotopes. Indeed, Table II shows that ω_3^0 is nearly the same for both (CH)$_x$ and (CD)$_x$ (~2040 cm^{-1}) while it reduces to ~1960 cm^{-1} for (^{13}CH)$_x$, i.e., approximately by the square root of the mass ratio of ^{13}C and ^{12}C. This means that the role of the hydrogen atoms in this mode is very small, and we therefore conclude that the heighest of the three *bare* modes considered here can indeed be identified as the C–C stretching mode. The frequency of this mode in the po-

lyacetylene chain is given by $\omega^2=2K/\mu$ where μ is the mode reduced mass. Taking μ as half the carbon atomic mass, we find the bare force constant (i.e., the contribution of the σ bond to the force constant) for this mode: $K=46$ eV/Å^2. This is the first experimental determination of the force constant for the bare carbon-carbon stretching mode. We emphasize that this estimate of K is a result of the amplitude-mode analysis (with an assumption on the value of the reduced mass) but does not involve *any* assumption on the nature of the dimerized state (e-e, e-ph, etc.). Our experimentally determined K can now be compared with the approximate values used in the literature. There have been two main ways to estimate K. One is to identify K with the force constant of the single-bond stretching mode of the ethane[23,42,43,57] which does not have any π electrons. For this mode ($\omega=993$ cm^{-1}) $d^2E_\sigma/dr^2=28$ eV/Å^2,[58,59] where E_σ is the σ-bond elastic energy and r is the vibration coordinate (the value $K=\frac{1}{4}d^2E_\sigma/dr^2=21$ eV/Å^2, which has frequently been used,[23,43,57] takes into account the projection of the bond direction on the chain axis). The other way is to identify K with the force constant of the totally symmetric A_{1g} mode of benzene which does not involve the π electrons;[45] for this mode $d^2E_\sigma/dr^2=47$ eV/Å^2 (Ref. 59) (r is now the bond direction), which is closer to our experimental value.

C. The e-ph interaction and the dimerization gap

The dimerization amplitude $\Delta_n=4\beta_n u_n$ for each mode is given by Eq. (4) and the total "dimerization gap" is defined by $2\Delta_d=2\sum\Delta_n$. Since in *trans*-polyacetylene $\lambda_3\gg\lambda_1,\lambda_2$ (see Table II), $\Delta_d\sim\Delta_3$. An estimate of Δ_d can be made using, for instance, the HS model[44] analyzed in Sec. V A. From Eq. (6) of Ref. 44 we have $\Delta_d/\Delta_0=(\Delta_0/2E_c)^\delta=0.78$, which means that the e-e interaction enhances the gap by about 30%. Similar estimates are obtained using the Hartree-Fock[43,46] or the Peierles-Hubbard[45] approximations. The e-ph interaction constant β_n for each mode can be expressed in the tight-binding approximation using Eq. (4) as

$$\beta_n^2=\pi t K_n \lambda_n/2 \ . \tag{48}$$

For the carbon-carbon stretching mode ($n=3$) we have $K_3=46$ eV/Å (see preceding section), $\lambda_3=\lambda_0(\lambda_3/\lambda_0)=0.12\times0.91=0.11$ (the value of λ_3/λ_0 is taken from Table II), and thus $\beta\sim\beta_3=4.3$ eV/Å for $E_c=4t=10$ eV. Earlier estimates[43,60,61] based on various data placed the value of β in the range 3.5–7 eV/Å. Using our derived values for β and Δ_d we estimate for the bond distortion $u=\Delta_d/4\beta\sim0.04$ Å in good agreement with the x-ray measurements of Fincher et al.[62]

D. The disorder

As was discussed in length in this work a critical experimental test for any model is the $\bar{\lambda}$-E_g relation. This relation yields the *type* of disorder, namely the functional dependence of $\bar{\lambda}$ (or the vibrational force constant) on the electronic gap E_g. We have shown that within the extended Peierls model a disorder mechanism in which the

intrinsic coupling parameters (*e*-ph and *e*-*e*) are varied, can account for the experimental data. Another type of disorder is observed in *trans*-$(CH)_x$ chains embedded in a partially isomerized sample [denoted $t(c)$].[63] In these samples the dispersion of the RRS lines with ω_L is much stronger, giving rise to a much steeper dependence of $\tilde{\lambda}$ on E_g. The disorder in $t(c)$ can be explained by a distribution in the extrinsic component of the gap, a component which does not exist in the ground-state degenerate all-*trans*-$(CH)_x$ but is present in *cis*-$(CH)_x$. The few *trans*-$(CH)_x$ chains embedded in the *cis*-$(CH)_x$ matrix acquire an extrinsic component Δ_e.

It has long been suggested that the disorder in *trans*-$(CH)_x$ originates from a distribution of "conjugation lengths." In this model the RRS frequencies are assumed to increase with decreasing conjugation length as in finite polyenes accounting thus for the dispersion with ω_L. Especially appealing in this model is the possibility to characterize the sample quality by an "average" length of the chains. However, as was discussed in Sec. II C, it is essential for any conjugation length model to include the variations of $\lambda(N)$ and $t(N)$. Numerical calculations of $\tilde{\lambda}$ for finite Huckel chains show that mainly a $\lambda(N)$ dependence could account for the data of Fig. 10, and the problem then reduces to the microscopic origin of this inhomogeneity. With a suitable $\lambda(N)$, data on *trans*-$(CH)_x$ seem compatible with a distribution $P(N)$ of conjugation lengths. However, it is not clear why in partially isomerized *trans*-$(CH)_x$ (Ref. 63) the slope of $\tilde{\lambda}_0/\tilde{\lambda}$ versus $\ln(\hbar\omega_L)$ would change from -0.37 (see Fig. 10 and Sec. III C) to -1.0; a change in $P(N)$ cannot readily account for this. Instead, a change in the type of disorder completely accounts for the data; the *cis*-induced disorder has the effect of finite odd chains breaking the $\Delta \rightarrow -\Delta$ degeneracy. If the length distribution were the main effect in all-*trans* we would expect to have even and odd chains, with the latter producing the much steeper slope in the $\tilde{\lambda}$ plot. The distinct behavior of $t(c)$ from all-*trans* thus indicates that chain-length distribution is not the main origin of inhomogeneity in all-*trans*. Also, contrary to the conjugation length model almost no dispersion of the RRS frequencies of the *cis*-$(CH)_x$ chains is observed in nearly all-*trans* samples where a distribution of *cis*-like chains is expected. On the other hand, in the AM model the extrinsic contribution to the gap in nondegenerate ground-state systems is taken into account, distinguishing thus between all-*trans* and partially isomerized $(CH)_x$. The fixed value of the extrinsic component in *cis*-$(CH)_x$ is probably the cause for the nondispersive RRS spectrum. Furthermore, it is observed[64] that as the temperature changes from 80 to 300 K, the primary and satellite frequencies shift in opposite directions. This is readily explained by the AM model as a result of opposite temperature dependence of the gap[49] and the bare phonon frequencies. The conjugation-length model, on the other hand, would predict that the primary and satellite shift in the same direction.

VI. SUMMARY AND CONCLUSIONS

We have shown that the resonant Raman data observed in *trans*-polyacetylene is due to scattering from amplitude

modes. A single-phonon propagator $D_0(\omega)$ accounts for all the observed phonon frequencies and relative intensities at all laser excitation energies. In disordered systems we have presented a method to derive the inhomogeneity distribution function $P(\tilde{\lambda})$ which describes the spatial variation of the gap and the dispersion of the RRS with $\hbar\omega_L$. We have found $P(\tilde{\lambda})$ which corresponds to our samples and have shown how to characterize other samples by the breadth of $P(\tilde{\lambda})$. We have also shown that the data provide the functional dependence of the gap on the coupling parameter $\tilde{\lambda}$, which is consistent with extended Peierls models including *e*-*e* interactions which enhance the gap by about 30%. The mechanism at the origin of the distribution $P(\tilde{\lambda})$ affects both the *e*-ph and *e*-*e* coupling parameters.

We have shown that the same phonon propagator $D_0(\omega)$ obtained from the Raman data determines also the charge-induced IRAV modes. A single pinning parameter α is needed to fix all phonon modes. It is found that $\alpha \sim 0.06$ for all photoinduced modes for all isotopes, whereas $\alpha \sim 0.23$ for doping-induced IRAV. The distribution function for the pinned charges is derived directly from the spectrum and is shown to be narrower for the photogenerated carriers.

We have provided evidence that the highest Raman and IRAV modes originate from the backbone C–C stretching mode. We have, for the first time, determined *experimentally* the σ-bond contribution to the C–C stretching force constant: $K = 46$ eV/$\AA^2$.

Finally, the amplitude-mode model is not limited, of course, to *trans*-polyacetylene and may be applied to various conjugation systems in which dimerization plays an important role. We have recently applied the ideas presented above to systems such as *cis*-$(CH)_x$ (Refs. 63 and 65) and partially isomerized *trans*-$(CH)_x$ (Ref. 63), and have shown the presence of amplitude modes in all of them. Preliminary analysis of polythiophene[66] and finite polyene chains such as β-carotene reveals that their phonon spectrum may also be described by amplitude modes.

APPENDIX A

In this appendix we evaluate the Raman cross section for the Peierls model. The relevant diagram is given in Ref. 29 and is evaluated in detail elsewhere.[67] Here we derive the result in the adiabatic limit $\omega \ll \omega_L$ by taking a derivative of the conductivity.[68]

The amplitude modes yield a time-dependent modulation of the gap of the form $\Delta + \delta(t)$, $\delta(t) \ll \Delta$. Since this time variation is slow (the adiabatic limit) one may consider the electronic conductivity of frequency ω_L to be time dependent with the form $\sigma(\omega_L, \Delta + \delta(t))$

$$\sigma(\omega_L, \Delta + \delta(t)) \simeq \sigma(\omega_L, \Delta) + \frac{\partial \sigma}{\partial \Delta} \delta(t) \ . \tag{A1}$$

An incident electric field $E \exp(i\omega_L t)$ leads to current oscillations of frequencies $\omega_L \pm \omega$, where $\delta(t) = \delta(\omega)\exp(i\omega t)$. This oscillating current radiates the Raman shifted power proportional to $|\partial\sigma/\partial\Delta \, \delta(\omega)|^2$. The $|\delta(\omega)|^2$ factor yields the dressed phonon propagator

$$D(\omega) = 2\lambda D_0(\omega)/N(0)[1 + (1-2\tilde{\lambda})D_0(\omega)]$$

(Ref. 67). The resonance effect is contained in the function $\partial\sigma(\omega_L, \Delta)/\partial\Delta$.

The conductivity $\sigma(\omega_L, \Delta)$ for the Peierls model (with electronic linear dispersion around the Fermi points) is known[11]

$$\sigma(\omega) = \frac{\omega_p^2}{4\pi i\omega}[g(\omega/2\Delta) - 1] , \qquad (A2)$$

where $\omega_p = [4\pi e^2 v_F^2 N(0)]^{1/2}$ is the plasma frequency and

$$g(x) = \begin{vmatrix} \left| \dfrac{1}{2x(x^2-1)^{1/2}} \right| \left| \ln \left| \dfrac{x-(x^2-1)^{1/2}}{x+(x^2-1)^{1/2}} \right| + \pi i \right| , & x > 1 \\[4mm] \left| \dfrac{1}{x(1-x^2)^{1/2}} \tan^{-1} \left| \dfrac{x}{(1-x^2)^{1/2}} \right| \right| , & x < 1 . \end{vmatrix}$$

$$(A3)$$

This excludes the phase-mode contribution,[11] which is absent in the present $\frac{1}{2}$-filled-band situation.

The radiation intensity $\sim \omega_L^2 |\sigma E|^2$ yields the Raman cross section

$$\frac{d^2\sigma}{d\Omega \, d\omega} \sim \omega_L^2 |\partial\sigma/\partial\Delta|^2 D(\omega) \sim (\lambda/\Delta^2)|f(\hbar\omega_L/2\Delta)|^2 D_0(\omega)/[1 + (1-2\tilde{\lambda})D_0(\omega)] , \qquad (A4)$$

where $f(x) = -x\partial g(x)/\partial x$ is given by Eqs. (23) and (24). Thus all the ω_L and Δ dependence, including the resonance effect at $\hbar\omega_L = 2\Delta$, are contained in $|f|^2/\Delta^2$. Direct diagrammatic evaluation of the cross section yields the same result when $\omega \ll \omega_L$ (Ref. 67).

APPENDIX B

The expressions for the coefficients c_1 and c_2/c_1 in the HS model[44] are given below,

$$c_1 = \frac{1 + (1-\lambda_0)\zeta/(1+\delta_0)}{1 - \left| \dfrac{\lambda_0}{\delta_0} - \dfrac{\lambda_0(\lambda_0+\delta_0)}{\delta_0^2} \ln \left| \dfrac{\lambda_0+\delta_0}{\lambda_0} \right| \right| \zeta} , \qquad (B1)$$

$$\frac{c_2}{c_1} = \frac{2\delta_0}{b} \left| \frac{1+\zeta}{\lambda_0\delta_0} + \frac{a}{b} \right| , \qquad (B2)$$

where

$$a = -\frac{\zeta^2}{\delta_0^2}\ln\frac{\lambda_0+\delta_0}{\lambda_0} + \zeta\frac{\lambda_0\zeta - \delta_0}{\delta_0\lambda_0(\delta_0+\lambda_0)}$$

$$+ \zeta\frac{\zeta+2}{2(\lambda_0+\delta_0)^2} - \frac{\delta_0^2+2\delta_0\lambda_0}{2\lambda_0^2(\lambda_0+\delta_0)}$$

and

$$b = \frac{\zeta}{\delta_0}\ln\left| \frac{\lambda_0+\sigma_0}{\lambda_0} \right| + \frac{\delta_0-\lambda_0\zeta}{\lambda_0(\lambda_0+\delta_0)} .$$

In the above equations λ_0 and δ_0 refer to the ordered state and ζ is the ratio between the first-order changes in δ and λ due to the inhomogeneity. ζ may formally be written as $\zeta = d\delta/d\lambda$.

The analogous expressions in the Hartree-Fock approximation[43,46] are as follows:

$$c_1 = \frac{1+v_0/\lambda_0}{1+\zeta}(1+2\zeta - v_0/\lambda_0) , \qquad (B3)$$

$$\frac{c_2}{c_1} = \frac{2\lambda_0(1+v_0/\lambda_0)(v_0/\lambda - \zeta)}{1+2\zeta - v_0/v_0} . \qquad (B4)$$

Similarly, λ_0 and v_0 refer to the ordered state while ζ can formally be written as $\zeta = dv/d\lambda$.

[1] I. Harada, Y. Furukawa, M. Tasumi, H. Shirakawa, and S. Ikeda, J. Chem. Phys. **73**, 4746 (1980).

[2] L. S. Lichtmann, A. Sarhangi, and D. B. Fitchen, Solid State Commun. **36**, 869 (1980).

[3] H. Kuzmany, Phys. Status Solidi B **97**, 521 (1980).

[4] S. Lefrant, J. Phys. (Paris) Colloq. **44**, C3-247 (1983).

[5] H. Kuzmany, Pure Appl. Chem. **57**, 235 (1985).

[6] E. Mulazzi, G. P. Brivio, E. Faulques, and S. Lefrant, Solid State Commun. **46**, 851 (1983); G. P. Brivio and E. Mulazzi, Chem. Phys. Lett. **95**, 555 (1983).

[7] R. Tiziani, G. P. Brivio, and E. Mulazzi, Phys. Rev. B **31**, 4015 (1985).

[8] L. Rimai, M. E. Heide, and D. Gill, J. Am. Chem. Soc. **95**, 4493 (1973).

[9] G. P. Brivio and E. Mulazzi, J. Phys. (Paris) Colloq. **44**, C3-261 (1983).

[10] H. Kuzmany, J. Phys. (Paris) Colloq. **44**, C3-255 (1983).

[11] P. A. Lee, T. M. Rice, and P. W. Anderson, Solid State Commun. **14**, 703 (1974).

[12] B. Horovitz, H. Gutfreund, and M. Weger, Phys. Rev. B **17**, 2796 (1978).

[13] M. J. Rice, Solid State Commun. **25**, 1083 (1978).

[14] B. Horovitz, Solid State Commun. **41**, 729 (1982).

[15] M. J. Rice, Phys. Rev. Lett. **37**, 36 (1976).

[16] C. R. Fincher, Jr., M. Ozaki, A. J. Heeger, and A. G. MacDiarmid, Phys. Rev. B **19**, 4140 (1979).

[17] J. F. Rabolt, T. C. Clarke, and G. B. Street, J. Chem. Phys. **71**, 4614 (1979).

[18]S. Etemad, A. Pron, A. J. Heeger, A. G. MacDiarmid, E.J. Mele, and M. J. Rice, Phys. Rev. B **23**, 5137 (1981).

[19]B. Francois, M. Bernard, and J. J. Andre, J. Chem. Phys. **75**, 4142 (1981).

[20]Z. Vardeny, J. Orenstein, and G. L. Baker, Phys. Rev. Lett. **50**, 2032 (1983).

[21]G. B. Blanchet, C. R. Fincher, T. C. Chung, and A. J. Heeger, Phys. Rev. Lett. **50**, 1938 (1983).

[22]E. J. Mele and M. J. Rice, Phys. Rev. Lett. **45**, 926 (1980).

[23]W. P. Su, J. R. Schrieffer, and A. J. Heeger, Phys. Rev. B **22**, 2099 (1980).

[24]S. A. Brazovskii, Zh. Eksp. Teor. Fiz. **78**, 677 (1980) [Sov. Phys.—JETP **51**, 342 (1980)].

[25]H. Takayama, Y. R. Lin-Liu, and K. Maki, Phys. Rev. B **21**, 2388 (1980).

[26]B. Horovitz, Phys. Rev. B **22**, 1101 (1980).

[27]B. Horovitz, Phys. Rev. Lett. **47**, 1491 (1981).

[28]Z. Vardeny, E. Ehrenfreund, O. Brafman, and B. Horovitz, Phys. Rev. Lett. **51**, 2326 (1983).

[29]B. Horovitz, Z. Vardeny, E. Ehrenfreund, and O. Brafman, Synth. Metals **9**, 215 (1984). (a) The factor λ/E_g^2 in Eq. (22) was not explicitly displayed in Refs. 28 and 29; (b) $f(x)$ in Ref. 29 has a misprint for $x > 1$.

[30]H. C. Longuet-Higgins and L. Salem, Proc. R. Soc. London, Ser. A **251**, 172 (1959).

[31]B. Horovitz, Mol. Cryst. Liq. Cryst. **120**, 1 (1985).

[32]F. B. Schugerl and H. Kuzmany, J. Chem. Phys. **74**, 953 (1981).

[33]B. Horovitz and J. A. Kurmhansl, Solid State Commun. **26**, 81 (1978).

[34]B. Horovitz, M. Weger, and H. Gutfreund, Phys. Rev. B **9**, 1246 (1974).

[35]D. Moses, A. Feldblum, E. Ehrenfreund, A. J. Heeger, T. C. Chung, and A. G. MacDiarmid, Phys. Rev. B **26**, 3361 (1982).

[36]P. M. Grant and I. P. Batra, J. Phys. (Paris) Colloq. **44**, C3-437 (1983).

[37]J. Ashkenazi, E. Ehrenfreund, Z. Vardeny, and O. Brafman, Mol. Cryst. Liq. Cryst. **117**, 193 (1985).

[38]I. I. Ukrainskii, Zh. Eksp. Teor. Fiz. **76**, 760 (1979) [Sov. Phys.—JETP **49**, 381 (1979)].

[39]P. Horsch, Phys. Rev. B **24**, 7351 (1981).

[40]S. Kivelson and D. E. Heim, Phys. Rev. B **26**, 4278 (1982).

[41]J. E. Hirsch, Phys. Rev. Lett. **51**, 296 (1983).

[42]S. N. Dixit and S. Mazumdar, Phys. Rev. B **29**, 1824 (1984).

[43]M. Grabowski, D. Hone, and J. R. Schrieffer, Phys. Rev. B **31**, 7850 (1985).

[44]B. Horovitz and J. Solyom, Phys. Rev. B **32**, 2681 (1985).

[45]D. Baeriswyl and K. Maki, Phys. Rev. B **31**, 6633 (1985).

[46]B. Horovitz and A. Krumhansl, Phys. Rev. B **29**, 2109 (1984).

[47]O. Brafman, Z. Vardeny, and E. Ehrenfreund, Solid State Commun. **53**, 615 (1985).

[48]We note here that the complete Raman spectra of *trans*-$(CH)_x$ contains also nonresonant lines which do not show the above dispersion and are therefore neglected below.

[49]Z. Vardeny, O. Brafman, and E. Ehrenfreund, Mol. Cryst. Liq. Cryst. **117**, 355 (1985).

[50]L. Lauchlan, Ph.D. thesis, University of Pennsylvania, 1982 (unpublished).

[51]L. Lauchlan, S. P. Chen, S. Etemad, M. Kletter, A. J. Heeger, and A. G. MacDiarmid, Phys. Rev. B **27**, 2301 (1983).

[52]J. Orenstein and G. L. Baker, Phys. Rev. Lett. **49**, 1043 (1982).

[53]J. Orenstein, G. L. Baker, and Z. Vardeny, J. Phys. (Paris) Colloq. **44**, C3-407 (1983).

[54]J. Orenstein, Z. Vardeny, G. L. Baker, G. Eagle, and S. Etemad, Phys. Rev. B **30**, 786 (1984).

[55]Z. Vardeny, J. Tanaka, H. Fujimoto, and M. Tanaka, Solid State Commun. **50**, 937 (1984).

[56]A. J. Heeger and A. G. MacDiarmid, Mol. Cryst. Liq. Cryst. **77**, 1 (1981).

[57]K. Fesser, A. R. Bishop, and D. K. Campbell, Phys. Rev. B **27**, 4804 (1983).

[58]Y. Ooshika, J. Phys. Soc. Jpn. **12**, 1238 (1957).

[59]T. Kakitani, Prog. Theor. Phys. **51**, 656 (1974).

[60]E. J. Mele and M. J. Rice, Solid State Commun. **34**, 339 (1981).

[61]H. Kuzmany, E. A. Imhoff, D. B. Fitchen, and A. Sarhangi, Phys. Rev. B **26**, 7109 (1982).

[62]C. R. Fincher, Jr., C.-E. Chen, A. J. Heeger, A. G. MacDiarmid, and J. B. Hastings, Phys. Rev. Lett. **48**, 100 (1982).

[63]Z. Vardeny, E. Ehrenfreund, O. Brafman, and B. Horovitz, Phys. Rev. Lett. **54**, 75 (1985).

[64]F. Coter, Z. Vardeny, E. Ehrenfreund, and O. Brafman, Synthetic Metals **17**, 331 (1986).

[65]E. Ehrenfreund, Z. Vardeny, O. Brafman, and B. Horovitz, Mol. Cryst. Liq. Cryst. **117**, 367 (1985).

[66]Z. Vardeny, E. Ehrenfreund, O. Brafman, A. J. Heeger, and F. Wudl, Synth. Metals **18**, 183 (1986).

[67]B. Horovitz, Z. Vardeny, E. Ehrenfreund, and O. Brafman, J. Phys. C **19**, 7291 (1986).

[68]G. W. Chantry, in *The Raman Effect*, edited by A. Anderson (Dekker, New York, 1971), p. 49.